Geophysical Journal International

Geophys. J. Int. (2022) **231,** 1750–1766
Advance Access publication 2022 July 26
GJI Marine Geosciences and Applied Geophysics

https://doi.org/10.1093/gji/ggac283

Performance of high-resolution impact and vibration sources for underground seismic exploration of clay formations at the scale of a rock laboratory

Britta Wawerzinek[1], Stefan Lüth,[1] Roman Esefelder[1,2] Rüdiger Giese[1] and Charlotte M. Krawczyk[1,2]

[1] *Helmholtz Centre Potsdam, GFZ German Research Centre for Geosciences, Telegrafenberg,* 14473 *Potsdam, Germany.*
E-mail: britta.wawerzinek@gfz-potsdam.de
[2] *Technical University Berlin, Ernst-Reuter-Platz* 1, 10587 *Berlin, Germany*

Accepted 2022 July 22. Received 2022 July 14; in original form 2021 June 29

SUMMARY

Low permeability, high retention capacity and self-sealing ability are advantageous characteristics that are attributed to argillaceous rocks. In contrast, other properties of clay, such as internal heterogeneities, strong attenuation and anisotropic behaviour, pose major challenges for underground exploration techniques. Although with regard to the underground storage of nuclear waste, the seismic exploration in the underground itself is of great importance to fill the gap between surface and borehole investigations. Furthermore, to prevent destruction of the host rock during exploration this demands low to non-invasive techniques. To approach these issues, a seismic survey was carried out in the Mont Terri Underground Rock Laboratory (Switzerland) using a gallery-based acquisition with an operating range up to several decametres. The seismic campaign included three-component borehole sensors and two different seismic source types (pneumatic impact and magnetostrictive vibroseis source). An executed source comparison analysed the characteristics of the different source types, for example frequency or amplitude behaviour of the generated wavefield, to assess their performance under similar conditions at the meso scale and to reveal their strengths and weaknesses in clay. Based on these findings, we performed traveltime and reflection analyses that demonstrate their potential to characterize clay formations and to map internal structures.

The highest seismic velocities are found in the carbonate-rich sandy facies ($v_{\mathrm{Pmax}} = 4000$ m s^{-1}, $v_{\mathrm{Smax}} = 2050$ m s^{-1}), slower velocities are found in the sandy facies ($v_{\mathrm{Pmax}} = 3720$ m s^{-1}, $v_{\mathrm{Smax}} = 1840$ m s^{-1}) and the slowest velocities are found in the shaly facies ($v_{\mathrm{Pmax}} = 3220$ m s^{-1}, $v_{\mathrm{Smax}} = 1480$ m s^{-1}). The seismic velocity anisotropy is larger within the shaly facies ($AvP = 23$ per cent, $AvS = 32$ per cent) compared to the sandy facies ($AvP = 9$ per cent, $AvS = 12$ per cent) and it is more pronounced for *S*-waves than *P*-waves. Thus, non-invasive meso-scale seismic techniques are suited to characterize the Opalinus Clay in great detail.

Key words: Time-series analysis; Controlled source seismology; Seismic anisotropy; Seismic attenuation; Seismic instruments; Wave propagation.

1 INTRODUCTION

The construction and safe operation of underground infrastructures, e.g. tunnels, mines, energy storage or repositories, depend on a detailed site characterization which is typically based on geological and geophysical investigations at the surface and in boreholes. However, surface investigations (e.g. 2-D/3-D seismics) are commonly used to explore large-scale structures to identify potential facility locations, but they lack resolution to appropriately characterize the host rock at the facility scale. In contrast, borehole measurements provide small-scale information, but only in the vicinity or between boreholes. To fill this gap in resolution and spatial coverage, near-surface or underground exploration is required. The site characterization for energy storage facilities or nuclear waste repositories additionally demands the application of low or non-invasive exploration techniques to avoid caprock and host rock destruction.

Various underground exploration approaches have been developed by the mining and tunnelling industry to explore the

surrounding rock mass units of a mine or a tunnel. However, underground exploration disturbs cost-intensive construction or production work, hence their interferences have to be minimal. For this reason, borehole and gallery-based acquisition systems have been developed enabling seismic exploration at metre to hectometre scale (Giese *et al.* 2005). Seismic measurements were applied in hard coal mining, exploiting the propagation of coal seam guided waves in order to detect discontinuities potentially affecting the safety of mining operations (Dresen 1985). More recent applications (Yancey *et al.* 2007) demonstrated the relevance of this method for detecting abandoned coal mines and voids therein that pose a potential risk of ground instabilities at the surface. In tunnel construction, various approaches have been developed for seismic exploration ahead of the tunnel while drilling. Tunnel seismic prediction (TSP; Dickmann & Sander 1996) or sonic softground probing (SSP; Kneib *et al.* 2000) were based on body-wave reflections whereby the body waves were generated by explosive sources in solid rocks or vibration sources in unconsolidated rocks. In contrast, seismic-while-drilling (SWD; Petronio & Poletto 2002) forwent external sources by using the noise of the tunnel boring machine (TBM) as a source signal. Newer concepts, for example integrated seismic prediction (ISP; Bäppler 2018), utilized tunnel to body-wave conversions (Bohlen *et al.* 2007; Lüth *et al.* 2008). In addition, software developments were further driven forward, e.g. pre-stack migration approaches (reverse time, Kirchhoff or Fresnel volume) to image heterogeneities ahead of the tunnel (Tzavaras *et al.* 2012; Cheng *et al.* 2014). During the operation of underground facilities, productivity or safety assessments are executed using seismic methods (Dales *et al.* 2017; Pisconti *et al.* 2020). In the Yima mining area (China), Cai *et al.* (2014) carried out an active seismic tomography to characterize the rock mass prior to extraction, followed by passive seismic tomography to monitor the extraction process.

Potential caprocks or host rocks for underground storage, e.g. energy storage or nuclear waste repositories, are salt, crystalline rock and claystone (IAEA 2009). The operation of underground research laboratories (URL) such as Grimsel, Aspö, Tournemire, Mont Terri etc. serves repository research (e.g. Bossart *et al.* 2017) with respect to: (1) characterization of host rocks, (2) development of barrier technology and (3) long-term safety assessment. Various applications in tunnel and mining settings demonstrate the suitability of the above-mentioned approaches for exploration, imaging and characterization of the host rock candidates crystalline rock and salt (e.g. Krauß *et al.* 2014; Richter *et al.* 2018). Claystone, the third host rock candidate, is attributed with low permeability, high retention capacity and self-sealing ability (Bossart *et al.* 2017). But it is also characterized by internal heterogeneities, strong attenuation, and anisotropy that present challenges for seismic underground exploration. Since the generated knowledge about clay is not directly transferable between clay formations (Mazurek *et al.* 2008), a detailed investigation of the site-specific structure and its effects on the wave propagation is required, especially in the context of site characterization of underground storage facilities. Seismic in situ measurements in clay formations contributed to the investigation of the excavation damaged zone (EDZ; Schuster *et al.* 2017; Schuster 2019; Leparoux *et al.* 2012), the characterization of clay (Zinszner *et al.* 2002; Manukyan *et al.* 2012; Zillmer *et al.* 2014), the detection of fault zones (Bretaudeau *et al.* 2014) and the monitoring of fluid migration (Rivet *et al.* 2016; Zappone *et al.* 2021). Monitoring concepts are essential in long-term safety assessment requiring high-resolution methods (Manukyan & Maurer 2020) and suitable acquisition systems to detect small changes early and reliably.

To tackle the challenging in situ clay exploration at the meso scale, a seismic experiment was conducted in the Mont Terri Underground Rock Laboratory (URL) using low-invasive methods. The survey aims at a high-resolution characterization of argillaceous formations (Opalinus Clay) by using visualization procedures, such as tomographic or reflection imaging. In addition, our campaign could be used as baseline to monitor effects of the excavation process of gallery 18 or the injection experiments CS-D and FS-B (Guglielmi *et al.* 2017; Zappone *et al.* 2021) on the undisturbed host rock. Accompanying the scientific aims, we utilized the acquired seismic data and performed a comparison of the different source types to investigate their characteristics in Opalinus Clay. This comprises (1) the investigation of the repeatability of the source signal, (2) amplitude and frequency analyses of the wavefield, including offset and directional dependences and (3) traveltime and reflection analyses to characterize the argillaceous rocks and image the structural elements around the URL. Knowing the influence of Opalinus Clay on the performance of the source types is essential to develop customized concepts for future acquisition in clay.

2 SETTING

2.1. Mont Terri Underground Rock Laboratory (URL)

A well-known test site to evaluate the suitability of new approaches and techniques for characterizing and monitoring of argillaceous formations is the Mont Terri Underground Rock Laboratory (URL). The URL (www.mont-terri.ch) is located north of St-Ursanne in the Swiss canton Jura next to the Mont Terri motorway tunnel. It lies within a clay formation of Toarcian/Aalenian age (approx. 174 Ma) with a thickness of ∼130 m and a rock overburden of ∼280 m (Bossart 2017). The bedding dips to SSE between 50° (S) and 30° (N). The Opalinus Clay contains a varying content of clay minerals, quartz, and carbonate that form three different facies types (Fig. 1): shaly, sandy, and carbonate-rich sandy facies (Jaeggi *et al.* 2017). The Opalinus Clay is characterized by a distinctive bedding anisotropy with lower velocity normal to bedding than parallel to bedding (Bossart 2017). In addition, the main fault passes through the centre of the URL and dips also to SSE between 40° and 55° (Jaeggi *et al.* 2017). For the last 25 yr, the following research objectives, among others, were investigated (Bossart 2017): (1) characterization of the Opalinus Clay (undisturbed host rock and EDZ); (2) interaction of host rock and barrier materials; (3) long-term safety assessment in terms of self-sealing of clay and migration of water or radionuclides. Therefore, various seismic measurements were applied, both in the laboratory and in situ.

The BGR (Federal Institute for Geosciences and Natural Resources, Germany) has performed several seismic in situ experiments at different scales, for example single borehole (IVM—interval velocity measurements) or crosshole measurement (XHM) as well as seismic transmission experiments (ST) to determine the seismic velocities and anisotropy of the different facies (Schuster *et al.* 2017). The borehole measurements (IVM) demonstrated the high variability of seismic velocities within the different facies types, for example $v_{P\perp} = 2800$–3700 m s^{-1} within the carbonate-rich sandy (crs) facies, or $v_{P\parallel} = 2600$–4600 m s^{-1} and $v_{P\perp} = 3200$–3800 m s^{-1} within the sandy facies (Schuster *et al.* 2017). IVM in the shaly facies resulted in average *P*-wave velocities of $v_{P\parallel} = 3030$ m s^{-1} and $v_{P\perp} = 2470$–2700 m s^{-1} and an anisotropy coefficient of $Av = 0.20$–0.23. The seismic transmission experiment revealed *P*-wave velocities of $v_{P\_crs} = 3990$ m s^{-1}, $v_{P\_shaly} =$

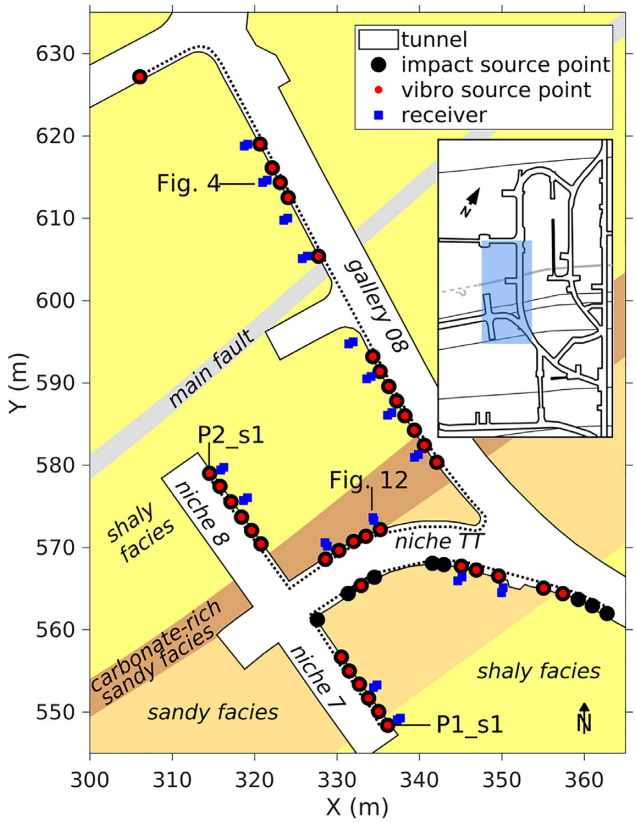

Figure 1. Map of the central part of the Mont Terri URL delineating the survey setup. The location of the survey is highlighted as blue area in the laboratory sketch. The dotted black lines outline the receiver gathers shown in Figs 4 and 12. The black solid lines point to the first shot point of each profile (P1_s1 and P2_s1) and the receivers displayed.

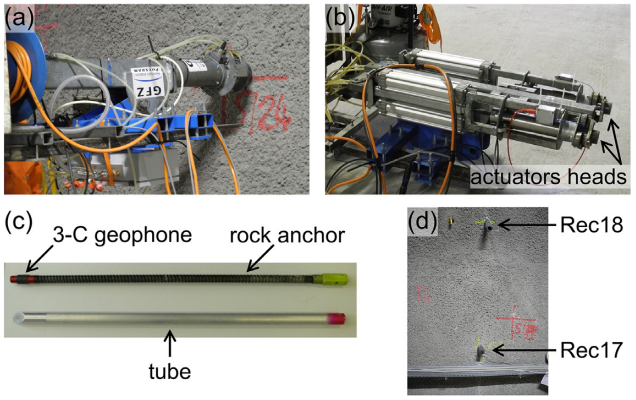

Figure 2. Photographs of the sources (a and b) and geophones (c and d). In operation, the pneumatic impact source (a) and the magnetostrictive vibroseis source (b) were mounted on a forklift (see Richter *et al.* 2018 for detailed engineering drawings). The 3-C geophones are mounted at the tip of 2 m long rock anchors (c) and were installed in boreholes (d).

3010 m s^{-1}, and v_{P_sandy} = 3410 m s^{-1} parallel to bedding (Schuster *et al.* 2017). Nicollin *et al.* (2008) have carried out a small-scale crosshole tomography of the EDZ in gallery 04. Their traveltime analysis derived seismic *P*-wave velocities of $v_{P\parallel}$ = 3330 m s^{-1} parallel to bedding and $v_{P\perp}$ = 2490 m s^{-1} normal to bedding. Slightly slower velocities ($v_{P\parallel}$ = 3110 m s^{-1}, $v_{P\perp}$ = 2340 m s^{-1}) were revealed with an anisotropic tomographic inversion of another crosshole survey (Manukyan *et al.* 2012) located approx. 30 m away. Crosshole measurements recently conducted below niche 8 (Zappone *et al.* 2021) determined significantly slower velocities ($v_{P\parallel}$ = 2870 m s^{-1}, $v_{P\perp}$ = 2280 m s^{-1}). During the excavation process of gallery 08, Le Gonidec *et al.* (2012) have performed active acoustic measurements as well as microseismic monitoring. The traveltime analyses of both experiments showed consistent *P*-wave velocities ($v_{P\parallel}$ = 3300 m s^{-1} and $v_{P30^\circ} \approx$ 3250 m s^{-1}) in the fast direction. In the slow direction, a velocity of v_{P70° = 2700 m s^{-1} was derived from the active experiment. Ultrasonic measurements at core samples in the laboratory confirmed the *P*-wave velocities of the shaly facies ($v_{P\parallel}$ = 3410 m s^{-1}, $v_{P\perp}$ = 2620 m s^{-1}) and revealed a seismic velocity anisotropy (*AvP*) of 25 per cent and a stronger shear wave velocity anisotropy (*AvS*) of 30–40 per cent (Popp & Salzer 2007). Wenning *et al.* (2021) analysed core samples from the vicinity of the main fault and found similar velocities ($v_{P\parallel}$ = 3340–3690 m s^{-1}, $v_{P\perp}$ = 2650 m s^{-1}) and anisotropy (*AvP* ~ 32 per cent) for the shaly facies beneath niche 8 (outside of the main fault). In contrast, ultrasonic measurements of core samples of the sandy facies resulted in higher velocities of $v_{P\parallel}$ = 3820–3860 m s^{-1} and $v_{P\perp}$ = 3280–3310 m s^{-1} (Gschwind 2013; Siegesmund *et al.* 2014), but revealed a weaker seismic velocity anisotropy *AvP* = 14–16 per cent (Siegesmund *et al.* 2014). The seismic velocities of the shaly facies derived by Popp & Salzer (2007), Nicollin *et al.* (2008), Le Gonidec *et al.* (2012) are consistent and the results of Siegesmund *et al.* (2014) and Gschwind (2013) agree completely as well. But their *P*-wave velocities are faster (~400 m s^{-1}) than those determined by Schuster *et al.* (2017). Lozovyi & Bauer (2018) performed dispersion analyses for the different facies types and they found a significant velocity variation by using ultrasonic (500 kHz) and seismic frequencies (0.5–150 Hz).

Up to now, the great majority of the seismic in situ experiments are reliant on boreholes and have covered the borehole or crosshole scale (metre scale). By using a gallery-based acquisition system, that explores the undisturbed rock from the easily accessible tunnel wall, a low to non-invasive approach was pursued. Utilizing source types designed for mining exploration increases the investigation scale to deca-/hectometres (meso-scale). Non-invasive exploration at the meso-scale is of great importance for long-term safety assessment of underground storage facilities or repositories.

2.2. Source specifications

We used a modular seismic acquisition and interpretation system, that unites technical developments with software implementations (Giese *et al.* 2005). The acquisition system contains two different source types, a pneumatic impact source and a magnetostrictive vibroseis source (Figs 2a and b, Table 1; see Richter *et al.* 2018 for details). The pneumatic impact source has a peak force of approx. 5 kg x 80 g = 3924 N ≈ 4000 N (1 g = 9.81 m s^{-2}) and generates impulse signals with a length of ~1 ms and a frequency range of 100–2000 Hz. The vibroseis source consists of two magnetostrictive actuators that can operate in *P*- or *S*-wave mode. In *P*-wave mode, both actuators oscillate in phase, operating as a vertical vibration source. In *S*-wave mode, both actuators oscillate inversely phased, whereby *P*-waves are eliminated and *S*- waves are enhanced (SHOVER technique of Edelmann 1981). The peak force is about 2 × 4270 N and the working frequency range of the sweep is mainly between 200 Hz to 14 kHz.

Table 1. Characteristics of the pneumatic impact and the magnetostrictive vibroseis source.

	Impact source	Vibroseis source	Vibroseis source in Mont Terri
Peak force	∼4000 N	2 × 4270 N	2 × 4270 N
Signal frequency	100–2000 Hz	200–14 000 Hz	100–1200 Hz
Signal length	1 ms		18 s

Table 2. Acquisition parameters of the seismic survey at the Mont Terri URL.

	Impact source	Vibroseis source
Period	January 2019	
Recording system	Distributed DAQlink 4 (Seismic Source Co)	
Receiver	2 × 16 3-C geophones (28 Hz)	
Sampling rate	0.25 ms	
Record length	500 ms	18 s + 1 s
Sweep frequency		100–1200 Hz
Sweep length		18 s
Source Points	45	37
Stacks per source point	5 hits	3 sweeps

2.3. Acquisition geometry and parameters

In January 2019, we carried out a low-invasive seismic survey (Mont Terri SI-A experiment, Table 2) that covered the galleries 04 and 08 as well as the niches TT, 7, and 8 (Fig. 1). In contrast to surface measurements, the gallery-based survey was conducted along the walls of the tunnel and not on the floor of the galleries. The survey aims at a spatial characterization of Opalinus Clay using imaging techniques in spite of a limited acquisition setup. But this campaign was also utilized to evaluate the performance of different source types (pneumatic impact source and the magnetostrictive vibroseis source, Figs 2a and b) in clay. Therefore, most of the source points were shot by both sources: The shaly and the carbonate-rich sandy facies were covered with the same source points (25), whereas the shot coverage varied in the sandy facies due to limited acquisition time. More shots were realized using the impact source (20) than the vibroseis source (12). The vibroseis source was operated both in *P*- and *S*-mode, hereinafter referred to vibroseis-*P* and vibroseis-*S*, and it excited a linear sweep from 100 to 1200 Hz with 18 s duration (flat amplitude spectrum). Due to the long excitation period, only 3 repetitions per source point were conducted in contrast to the 5 hit repetitions of the impact source.

The emitted source signals were recorded on 32 three-component geophones with a natural frequency of 28 Hz. The geophones were fixed at the tip of 2 m long rock anchors (Fig. 2c) which were screwed into tubes glued with epoxy to the anchor boreholes. Due to that the geophones are well coupled in all three dimensions to the rock and the borehole setup reduces the effect of ambient noise. A sheathing with PUR foams at the end of the geophone anchors reduces the entry of airborne sound waves in the receivers (Fig. 2d). The receivers were vertically spread over two levels 2 m apart (Fig. 2d) and the lower sensors were oriented horizontally (w/o inclination), while the upper sensors had an inclination of 40°. This setup was chosen for the structural imaging approach. Because of this, the component orientations of the upper and lower sensors differ which means that mainly the lower sensors (w/o inclination) are included in the amplitude and frequency analyses. The individual components of the lower receivers were oriented vertically, perpendicular and parallel to the tunnel wall.

3 SOURCE COMPARISON

3.1. Data pre-processing

Since this study focuses on the comparison of the impact and the vibroseis sources and their performance in clay formations, the different data sets required a comparable data processing. The pre-processing of the vibroseis data involved only few needful steps: (1) the vibroseis correlation with the synthetic sweep which is fed into the source, (2) bandpass filtering (BP 80–100–1200–1300Hz) to remove the strong electrical noise (50 Hz), (3) vertical stacking to improve the signal-to-noise ratio, and (4) a minimum phase transform that was only applied for first break onset picking. The pre-processing of the impact data included steps (2) and (3): bandpass filtering for reasons of comparability with the vibroseis data and vertical stacking. The data processing, which was required for the structural imaging, is specified in Section 3.8.

The source comparison contains several analyses that were performed using different fractions of the data set. The evaluation of the source signal repeatability as well as the clay characterization was based on the complete data set, which includes all receivers (upper and lower) and covers all facies areas. In contrast, the amplitude and frequency analyses were carried out using only the lower receivers without inclination. Additionally, we focused on the northern part of the survey (i.e. shaly and crs facies) because of the higher number of shots and the similar shot locations; the rectangular layout simplified the component assignment (radial and transverse). In the following this data subset is referred to as 'shaly-crs data set'.

3.2. Repeatability of source signals

To evaluate the repeatability of both sources and their emitted signals, the individual excitations (hits and sweeps) at each source point were analysed prior to vertical stacking. To focus on the source signal and the ambient noise level during the measurements, correlation coefficients (*CC*, Fig. 3a) of the individual shots were calculated for a 55 ms long time window around the *P*-wave onset ($t_P - 5$ ms $\leq t \leq t_P + 50$ ms). At each shot point, the vibroseis source excited almost identical source signals, although the source signals in *S*-mode (median(CC_S) = 0.9861) differ slightly more than the source signals in *P*-mode (median(CC_P) = 0.9972). The differences between the individual shot recordings are presumably caused by uncorrelated ambient noise. In contrast, we noticed a different behaviour of the impact source. The first hit has a time-shift of up to ∼1 sample and lower amplitudes than the following impact hits. The correlation between the first hit and hits 2 to 5 yields coefficients (median($CC_{1\text{-}5}$) = 0.8528) that are significantly smaller than the correlation between hits 2 to 5 among themselves (median($CC_{2\text{-}5}$) = 0.9901). However, it seems that the influence of the first hit in the vertical stacking is less than anticipated, since the resulting vertical stacks with and without first hit are almost the same (Fig. 3b, median(*CC*) = 0.9948). Therefore, we stack all 5 impact hits per source point. In comparison, the source repeatability of the vibroseis source is slightly higher than of the impact source due to the applied signal phase and amplitude control system

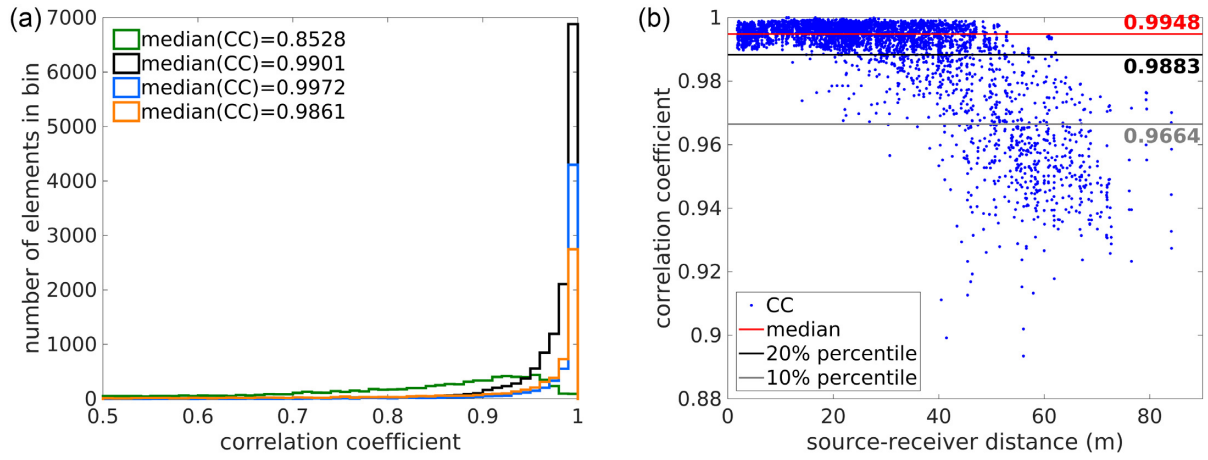

Figure 3. Source signal repeatability. (a) Comparison of the correlation coefficients (*CC*) of the individual shots at each source point before vertical stacking. Legend: green—correlation between the first impact hit and hits 2–5; grey—correlation between impact hits 2–5; blue—correlation between vibroseis-*P* sweeps 1–3; orange—correlation between vibroseis-*S* sweeps 1–3. (b) Correlation between the vertical stacks of impact hits 1–5 and impact hits 2–5 using all source-receiver combinations. The analysed time windows are (a) $t_P - 5$ ms $\leq \; t \leq t_P + 50$ ms and (b) $0 \leq t \leq 150$ ms.

(Richter *et al.* 2018). In general, both sources demonstrate a high repeatability of the source signal.

3.3. Comparison of seismic traces

The ambient noise conditions in the Mont Terri URL were good during the measurements, although drilling work was performed some decametres (∼100 m) away. Nonetheless, the raw impact data (w/o BP filter) show a very low noise level, compared to the vibroseis data that are highly affected by interferences, for example electrical noise (50 Hz). After applying a bandpass filter (80–100–1200–1300 Hz), which represents the frequency response of the sweep, the noise on the vibroseis data is reduced, but it is still slightly higher compared to the impact data. For reasons of comparability, the impact data were bandpass filtered as well. Fig. 4 shows exemplarily a typical receiver gather of the bandpass filtered impact and vibroseis-*P* data. Some differences are directly deducible from the seismic traces. The impact source generated clearer signals with stronger lower frequencies than the vibroseis-*P* source, whose signals are dominated by higher frequencies. The *P*- waves generated by both sources are visible at all stations. Both sources also excited shear waves, but the shear waves generated by the vibroseis-*P* source are weaker and only traceable at shorter source-receiver distances than those generated by the impact source. To generate shear waves with the vibroseis source in *S*-mode both actuators oscillate inversely phased (Edelmann 1981) changing the ratio of the *P*- and *S*-wave energy towards the shear waves. However, this approach is not working equally well at all source points. For example, receiver gather 29 (Fig. 4) shows an enhancement of shear waves on both components for source points 23 to 31, while it is not observed at the others. This might be caused by heterogeneities e.g. in the vicinity of the source (2 heads) which disturb uniform interferences in all directions and thus prevent an optimal amplification or elimination of the wave types.

3.4. Signal-to-noise ratios

In order to compare the quality of the different sources, the signal-to-noise ratios (SNRs, eq. 1) were determined. The SNRs were calculated for the radial components of the shaly-crs data set (Section 3.1). The calculation itself followed Staples *et al.* (1999), Yordkayhun *et al.* (2009) and Sopher *et al.* (2014):

$$\mathrm{SNR} \; = \mathrm{rms}\,(\mathrm{signal})\,/\mathrm{rms}\,(\mathrm{noise})\,. \qquad (1)$$

The rms amplitude of the signal was computed in a 50 ms long time window around the *P*-onset ($t_P \leq t \leq t_P + 50$ ms), whereas the time window from 100 to 150 ms was used to determine the rms amplitude of the noise. This time window was chosen, because no coherent signals were visible and its noise level is comparable to the noise level before the first breaks.

The signal-to-noise ratio (Fig. 5) is offset dependent and decreases with increasing offset. For the frequency ranges that comprise the whole useful signal (Figs 5a and b) applies that the impact source has the highest SNR, followed by the vibroseis-*P* source and then the vibroseis-*S* source with the lowest SNR. The SNR of the impact source is significantly higher in the frequency range of 100–300 Hz (Fig. 5c) compared to the other frequency ranges (100–1200, 300–800, 600–1200, 1200–1800 Hz). Frequencies below 300 Hz are associated with highest shear and tunnel wave amplitudes and lowest noise amplitudes which explains the high SNR in the frequency range of 100–300Hz. The SNR of the impact and vibration source (vibroseis- *P* and vibroseis-*S*) are similar in the high-frequency range 600–1200 Hz (Fig. 5d), but the vibration source shows higher SNR for frequencies >1200Hz (Fig. 5e). However, that is associated with the strong amplitude decay of the impact data above 800 Hz (Fig. 6).

3.5. Frequency content

3.5.1 Frequency analysis

To analyse the frequencies generated by the different source types, the shaly-crs data set (Section 3.1) was used to compute averaged amplitude spectra (Margrave 2021) in the time window from 0 to 150 ms. The resulting amplitude spectra of the three sources vary in shape (Fig. 6). The mean amplitudes of the impact and vibroseis-*P* source decrease with increasing frequency in contrast to the vibroseis-*S* source, that shows an amplitude increase with increasing frequency. However, the vibroseis-*S* amplitude is only half of the vibroseis-*P* amplitude presumably due to the different

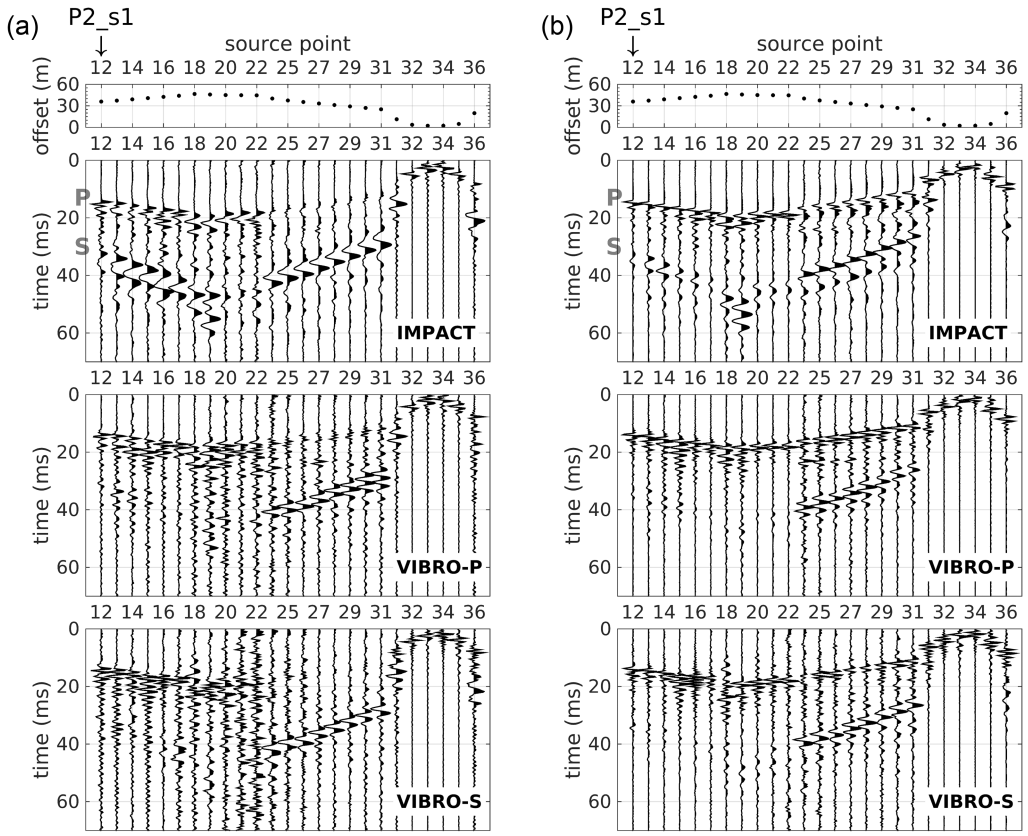

Figure 4. Receiver gather example of the impact, vibroseis-*P* and vibroseis-*S* data with source-receiver distances of 2–47 m. The example shows the tunnel-radial (a) and tunnel-parallel (b) component. The data processing comprised bandpass filtering (80–100–1200–1300Hz) and trace normalization. The first shot point of the profile is marked by the arrow; see Fig. 1 for receiver and profile locations.

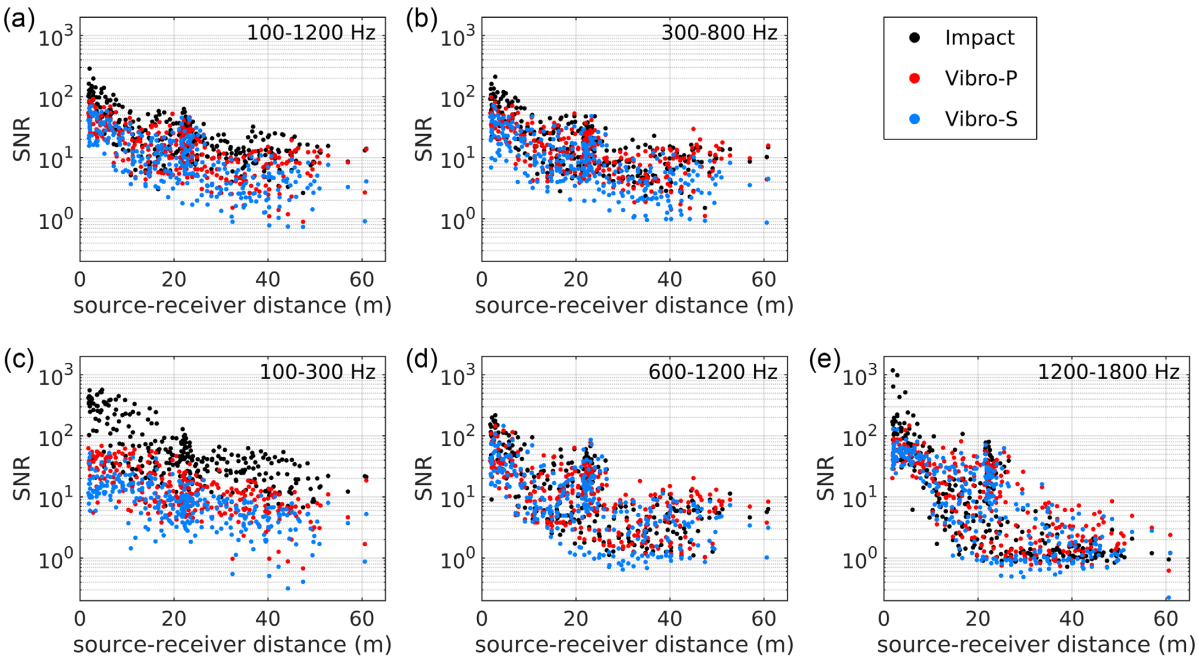

Figure 5. Signal-to-noise ratio (SNR) of impact (black), vibroseis-*P* (red) and vibroseis-*S* (blue) data for different frequency ranges: (a) 100–1200 Hz, (b) 300–800 Hz, (c) 100–300 Hz, (d) 600–1200 Hz and (e) 1200–1800 Hz. For lower frequencies (a–c), the impact data show generally higher SNRs than the vibroseis data.

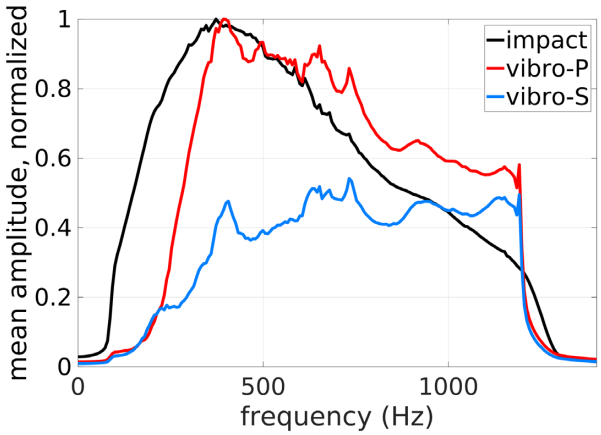

Figure 6. Average amplitude spectra of impact (black), vibroseis-*P* (red) and vibroseis-*S* (blue) data after applying a bandpass filter (80–100–1200–1300 Hz). The impact spectrum is normalized to its maximum, while vibroseis-*P* and vibroseis-*S* spectra are normalized to maximum of the vibroseis-*P* data. The impact data show generally stronger lower frequencies than the vibroseis data.

oscillation of the actuators operating in *P*-mode (in phase) and *S*-mode (inversely phased). The −3 dB points were determined to obtain the dominant frequency range and the 3-dB bandwidth. The *P* sources have comparable bandwidths, but the impact source (485 Hz) has a slightly broader bandwidth than the vibroseis-*P* source (460 Hz). The dominant frequency range of both sources overlap, but the impact source generates lower frequencies (195–680 Hz) than the vibroseis-*P* source (320–780 Hz). However, the vibroseis-*P* data also show that the pre-defined frequency range (sweep up to 1200 Hz) is not fully recovered, amplitudes above 800 Hz are strongly attenuated. This relative amplitude decay at higher frequencies (>800 Hz) is stronger for the impact data than the vibroseis-*P* data. In contrast to the *P*-sources, the vibroseis-*S* source presents a broader bandwidth (770 Hz) divided in two frequency ranges of 370–440 Hz and 490–1190 Hz. Although the pre-defined sweeps started at 100 Hz, frequencies below 350 Hz, that are essential for shear wave propagation, are missing in the recorded signals generated by the vibroseis source operating in *P*- and *S*-mode (Fig. 6). The limited performance below 300 Hz is caused by the construction of the actuators that defines their lower characteristic line. With great effort the source can operate below this line, but interferences can occur simultaneously. The analysis of the frequency content of the different source types emphasizes their advantages: (1) The impact source excites strong low-frequency signals and (2) the vibroseis source excites signals with a higher frequency content. By specifying the sweep frequencies and real time steering of the actuators the frequency content of the signals is better controlled, especially in the high-frequency range. However, the frequency analysis also shows that frequencies above 800 Hz are strongly absorbed by the clay formation.

3.5.2 Offset and directional dependence

Since claystone is known for its strong attenuating and anisotropic behaviour, we analysed the frequency content in dependence of offset and propagation direction to describe the site-specific clay formation. At first, we studied the offset dependence and for this purpose, we divided the offset range into ten 5 m (offset 0–50 m) and two 10 m bins (offset 50–70 m). Then, we calculated the average amplitude spectra using only radial components of shaly-crs data (Section 3.1). This approach shows the same result for impact and vibroseis-*P* data: The amplitude decreases with increasing offsets up to 30 m, while larger offsets present comparable amplitude spectra. Since higher frequencies are stronger affected than lower frequencies, the dominant frequency shifts towards lower frequencies.

In the second step, we analysed the individual amplitude spectra of the shaly-crs data in terms of (1) directional dependence in each offset bin and (2) offset dependence in each azimuth bin (Fig. 7). The (source-receiver) azimuth is defined as the angle of the connecting line from source to receiver relative to north. The above-mentioned offset dependence is clearly visible in all azimuth bins and Fig. 7(b) shows exemplarily the azimuth bin 165–195°. With increasing offset, the amplitude decreases with a stronger decay at higher frequencies, yielding steeper inclined spectra and lower dominant frequencies. In contrast to that, the directional dependence is not uniform. Mostly, we observe no directional dependence, except for offsets from 20 to 25 m (Fig. 7a), the offset range that comprise the best azimuthal coverage. There, dropping spectra are visible for the azimuth range of 135–165° and 315–345°, while the residual azimuth ranges have flat spectra, indicating lower frequencies normal to bedding. This behaviour can be seen for all sources, but it is very pronounced for the impact data (Fig. 7).

3.6. Energy content

3.6.1 Amplitude analysis

To analyse the energy content excited by the impact and the vibroseis-*P* source, we compare the relative offset-dependent amplitude reduction of the sources to each other. Therefore, the rms amplitudes of the *P*-waves were calculated, normalized to the maximum rms amplitude of each data set and plotted over source-receiver distance (Fig. 8). The time window was generally 5 ms long, but in the near-offset range, the time window was narrowed and stopped at the *S*-wave onset. As expected, the amplitudes of both source types are rapidly decreasing in the near-offset range. At distances larger than 6 m the rms amplitudes are less than 10 per cent of their maximum. The rms amplitudes are even smaller than 1 per cent at distances larger than 30 m. Both sources show a similar decrease, although the variation of the rms amplitudes of the vibroseis-*P* data is stronger in the far field than those of the impact data. Despite the strong amplitude reduction, only 3 per cent of impact and 17 per cent of vibroseis-*P* data show a signal-to-noise ratio lower than 5 (Fig. 5a). In terms of penetration depth for claystone, we infer from this that the energy generated by both source types is fully sufficient for the seismic transmission up to at least 65 m. The penetration depth can certainly be larger, since we also observe *P*- waves at distances up to 84 m: For example, *P*-waves, that were generated at the remote shot point in the north, were recorded on receivers, that were placed in the sandy facies (Fig. 1). In addition, we observe reflected shear waves, whose reflections occurred at a distance of ∼50 m (*cf.* Section 3.8).

3.6.2 Attenuation

One method to estimate the attenuation characteristics of a medium in the frequency domain is the logarithmic-spectral-ratio method (LSR; Johnston *et al.* 1979; Toksöz *et al.* 1979). The attenuation, that is described by the quality factor Q, is defined as the ratio of

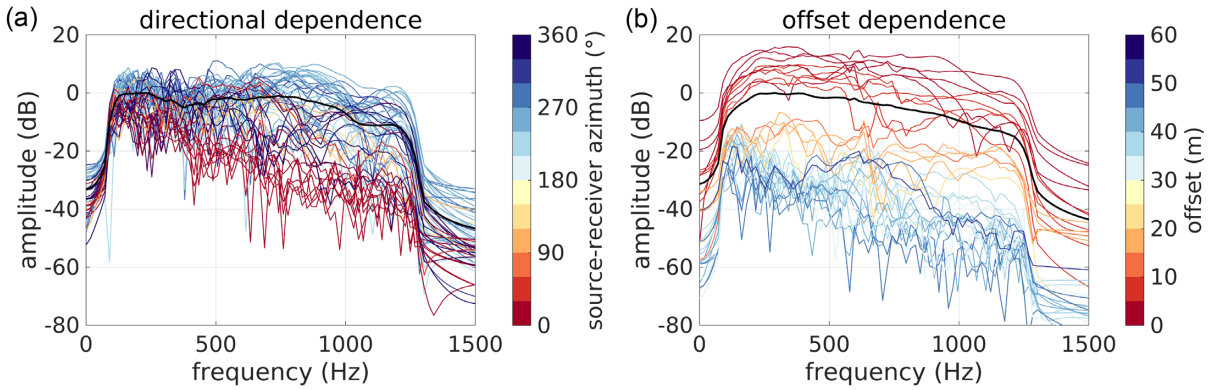

Figure 7. Amplitude spectra of impact data in dependence of source-receiver azimuth (a) and offset (b), after applying a bandpass filter (80–100–1200–1300 Hz) and using a 55 ms long time window around the *P*-onset ($t_P - 5$ ms $\leq t \leq t_P + 50$ ms). The directional dependence is shown for the specific offset range of 20–25 m and the offset dependence is exemplarily shown for the azimuth range of 165–195°. The azimuth and offset are colour coded and the average amplitude spectrum is plotted in black.

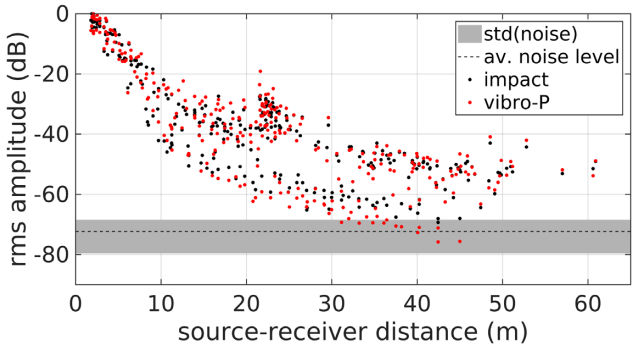

Figure 8. Rms amplitudes in dependence of source–receiver distance of the impact (black dots) and the vibroseis-*P* (red dots) data. The rms amplitude was computed for a 5 ms long time window around the *P*-wave onset. In the near-offset range, the time window was narrowed and stopped at the *S*-wave onset. For comparison, we included the mean noise level (dashed line) with its standard deviation (grey area) computed for a time window of 10 ms prior the *P*-wave onset.

two frequency spectra, namely source spectrum $S(x, f)$ and receiver spectrum $R(x, f)$. For more details see Krauß *et al.* (2014);

$$\ln(R(x, f)/S(x, f)) = -(\pi d)/(Qv)\, f + \ln(R(x)/S(x)) \quad (2)$$

$$\alpha = -(\pi d)/(Qv) \quad (3)$$

$$Q = -(\pi t_P)/\alpha \quad (4)$$

The quality factor Q (eq. 2) is estimated by the slope α (eq. 3) of the logarithmic spectral ratio plotted over the frequency. The slope α is calculated by a linear regression in the frequency range of 100–1200 Hz for the impact source and 300–1200 Hz for the vibroseis-*P* source. The quotient of travel distance d (source-receiver distance Δx) and velocity v is approximated ($d/v = \Delta x/v = \Delta t$; Tonn 1991) with the *P*-onset time t_P.

At first, the source signals and their spectra were determined. The synthetic sweep, the signal which is fed into the source and steers the actuators, was used as the vibroseis-*P* source signal. Since neither a pilot signal nor a general source signal was available for the impact source, its source signal was approximated. Amplitude spectra of near-offset recordings (offset < 3 m) were computed from a 3.5 ms long time window around the *P*-onset ($t_P - 0.5$ ms $\leq t \leq t_P + 3$ ms) and then averaged to obtain the source spectra. The receiver spectra were yielded by the amplitude spectra of individual traces in a 55 ms long time window around the *P*-onset ($t_P - 5$ ms $\leq t \leq t_P + 50$ ms). To obtain more stable results but also to consider a potential dependence on the rock condition (EDZ, undisturbed rock), the individual receiver spectra were at first binned by ray length (bin size 5 m), then component-wise averaged and finally summed. In the next step (Fig. 9), the natural logarithm of the ratio of receiver and source spectrum was computed and the slope α was determined. In the last step, Q was estimated using eq. 4 with the individual traveltimes, before its median was computed.

The resulting Q estimates (Fig. 10a) increase with increasing ray length, where a longer ray length indicates a longer ray path through the undisturbed rock. In general, the estimates of Q of the vibroseis-*P* data are higher than those of the impact data. The vibroseis-*P* data show a stronger variation of the Q values, especially for ray lengths of 20–30 m, where $Q_{\text{vibroseis-}P}$ are much higher than Q_{impact}. In contrast, the impact data display a strong jump of Q at ∼20 m. Ray lengths up to 20 m, Q has values below 15 and above 20 m the Q values are between 15 and 25. This jump presumably indicate that we estimate Q values affected by the EDZ (damaged rock, short ray length) and Q values characterizing the undisturbed rock (long ray length) of the Opalinus formation. Despite the approximations made for the impact source signal, the resulting Q values from impact and vibroseis-*P* data match unexpectedly well. Since we still observe clear deviations between both source types, we do not interpret the exact Q values but rather their range. The great majority of Q is clearly lower than 25 with a median of Q_{impact} of about 16. By analysing the impact data set separately according to facies type, the influence of the shaly facies becomes apparent (Fig. 10b).

3.7. Suitability for clay characterization (traveltime analysis)

Traveltime analyses of all data sets (impact, vibroseis-*P* and vibroseis-*S*) were performed to determine the seismic velocity structure of the claystone formation and thereby to evaluate the suitability of the different source types for clay characterization at the mesoscale. The first break onsets of the *P*- and *S*-waves were picked and the average velocities were derived for straight rays. To characterize the different facies types separately, only ray paths that propagated through one facies type were considered further on. In addition, near-offset shots were excluded as well, since their pick uncertainties can cause large velocity errors. In order to focus on

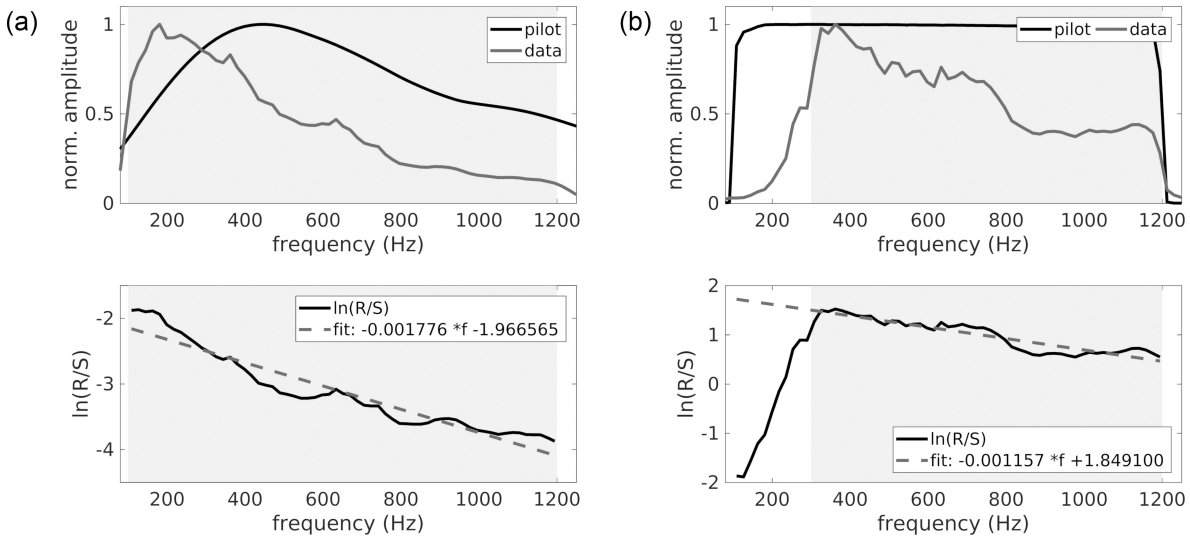

Figure 9. Logarithmic spectral ratio (LSR) example of the impact (a) and the vibroseis *P*-data (b). Top: normalized amplitude spectra of the source (black) and the receiver (grey) signals. Bottom: logarithmic spectral ratio (black) and corresponding linear fit (grey). The frequency ranges used are marked by the light grey areas. The predefined sweep was used as the vibroseis source signal, while the impact source signal was approximated as the average amplitude spectrum of the nearest offset recordings (offset < 3m). The amplitude spectra of the receivers were averaged for offset bins with a size of 5 m.

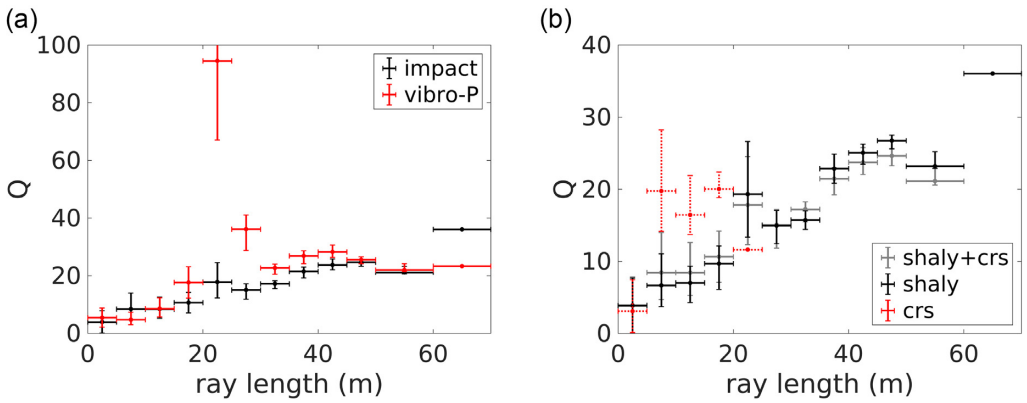

Figure 10. (a) Quality factors (Q) of the impact (black) and the vibroseis-*P* (red) data and (b) quality factors (Q) of the different facies types estimated using the impact data. At first, the individual Q values were determined by using the LSR method (Fig. 9) and then the median Q values were calculated for each ray length bin (size: 5 m, horizontal bar). The vertical bars mark the range from $Q_{\min}$ to $Q_{\max}$ in each offset bin. The significant different Q (below and above 20 m) are presumably caused by different rock conditions (EDZ, undisturbed rock). To emphasize the higher uncertainty of Q_{crs} (b) their error bars are plotted as dotted line.

the characterization of the undisturbed rock, picks from waves that propagated only through the EDZ, e.g. waves from the shots in niche 8 to the receivers in the same niche, were excluded too. After applying these selection criteria 332 of 760 (43.7 per cent) impact source-receiver combinations and 288 of 696 (41.4 per cent) vibroseis source-receiver combinations remain. The resulting clay characterization is based on 76–100 per cent of these selected combinations (Table 3), whereby more usable *P* picks are available than *S* picks. The great majority of rays pass the shaly or the sandy facies, while the crs facies is covered by only few rays. Combined with its limited azimuthal coverage, the carbonate-rich sandy facies characterization is less reliable than those of the shaly and sandy facies. To investigate the anisotropic behaviour of clay (Fig. 11), the average velocities were plotted in dependence of the source-receiver azimuth and an ellipse was fitted (Gal 2003, modified). That approach led to estimations of the maximum and minimum velocity as well as the angle of the fast velocity axis (Tables 4 and 5). Afterwards, these values were used to derive the anisotropy coefficients (Av, eq. 5) and the seismic velocity anisotropy AvP (eq. 6) and AvS (eq. 7) according to Schuster *et al.* (2017) and Birch (1961).

$$Av = (v_{max} - v_{min})/v_{min} \tag{5}$$

$$AvP = (v_{Pmax} - v_{Pmin})/v_{Pmean} \tag{6}$$

$$AvS = (v_{Smax} - v_{Smin})/v_{Smean} \tag{7}$$

The average *P*- and *S*-wave velocities illustrate a clear azimuthal dependence and significant velocity contrasts between the facies types (Fig. 11). Without considering any anisotropy the fastest v_{P} and v_{S} are measured in the carbonate-rich sandy facies. Slower velocities are found in the sandy facies and the slowest velocities are observed in the shaly facies (see mean and median values in Tables 4 and 5). The derived seismic *P*-wave and *S*-wave velocities ($v_{\max}$, $v_{\min}$, v_{mean}) of the impact and vibroseis data differ from each other

Table 3. Number of *P* and *S* picks used for clay characterization after near-offset shots and EDZ rays were excluded and only ray paths through one facies type were considered.

Source type	Shaly	Sandy	crs	Total	
impact	P: 211/211	P: 96/96	P: 25/25	P: 332/332	100%
	S: 191/211	S: 96/96	S: 24/25	S: 302/332	91%
vibroseis *P* mode	P: 211/211	P: 52/52	P: 25/25	P: 288/288	100%
	S: 165/211	S: 52/52	S: 19/25	S: 236/288	82%
vibroseis *S* mode	S: 162/211	S: 40/52	S: 16/23	S: 218/286	76%

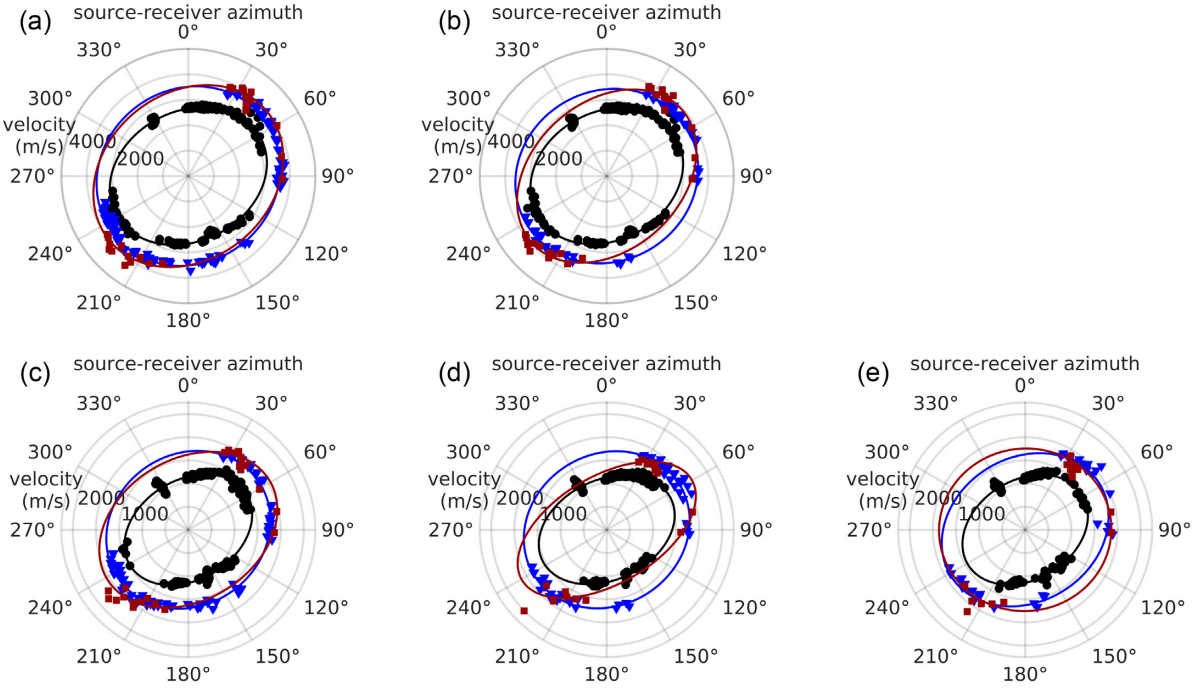

Figure 11. Azimuthal distribution of *P*-wave (a and b) and *S*-wave (c–e) velocities of the impact data (a and c), the vibroseis-*P* data (b and d) and vibroseis-*S* data (e) after near-offset shots were excluded. Elliptical fitting was applied to determine v_{max}, v_{min} and tilt (Tables 4 and 5). The source–receiver combinations were grouped by facies types: red squares—carbonate-rich sandy facies; blue triangles—sandy and (few) upper shaly facies; black—lower shaly facies including far-offset shots.

Table 4. *P*-wave velocity derived from straight rays and fitting an ellipse to the data. Median of v_P is calculated from the individual v_P data without ellipse fitting and consideration of anisotropy. Poorly adapted values are italicized.

Source type	Facies	v_{Pmax} (m s^{-1})	v_{Pmin} (m s^{-1})	tilt (°)	v_{Pmean} (m s^{-1})	$v_{P\,median}$ (m s^{-1})	*Av*	*AvP*
Impact	**shaly**	**3217**	**2551**	**63**	**2884**	**2759**	**0.261**	**0.231**
	sandy	**3724**	**3403**	**53**	**3564**	**3626**	**0.094**	**0.090**
	crs	**4004**	***3271***	***51***	***3638***	***3885***	***0.224***	***0.202***
Vibroseis	shaly	3140	2515	61	2828	2719	0.246	0.221
P mode	sandy	3678	3341	60	3510	3609	0.101	0.096
	crs	3943	*2912*	*49*	*3428*	*3800*	*0.354*	*0.301*

with about 100 m s^{-1}, but larger variations occur for the carbonate-rich sandy facies. However, the individual velocity differences can be larger: We observe rms deviations of 2–5 per cent for *P*-wave velocities and 2.5–10 per cent for shear wave velocities. Noisy traces and error-prone picks in the correlated vibroseis data cause these pick inaccuracies. A velocity error of 100 m s^{-1} at a velocity of 3000 m s^{-1} (∼3 per cent) and a distance of 30 m can be caused by a pick inaccuracy of approx. 0.25 ms or 1 sample. Since a pick uncertainty of 1 sample is realistic, the derived seismic velocities of impact and vibroseis data are in good agreement. The impact data demonstrate the best data quality for picking as well as the highest number of *P* and *S* picks. Therefore, the impact data set is used for further consideration and interpretation. The resulting first break onsets and the derived seismic anisotropy of the impact data embody the input data for a tomographic imaging of the Opalinus Clay (Esefelder *et al.* 2021).

The azimuthal dependence of the seismic *P*- and *S*-wave velocities is clearly visible in the impact data (Figs 11a and c). The fast

Table 5. *S*-wave velocity derived from straight rays and fitting an ellipse to the data. Median of v_S is calculated from the individual v_S data without ellipse fitting and consideration of anisotropy. Poorly adapted values are italicized.

Source type	Facies	v_{Smax} (m s^{-1})	v_{Smin} (m s^{-1})	tilt (°)	v_{Smean} (m s^{-1})	$v_{Smedian}$ (m s^{-1})	*Av*	*AvS*
Impact	**shaly**	**1477**	**1074**	**59**	**1276**	**1177**	**0.375**	**0.316**
	sandy	**1843**	**1630**	**55**	**1737**	**1775**	**0.131**	**0.123**
	crs	**2054**	***1524***	***59***	***1789***	***1916***	***0.348***	***0.296***
Vibroseis	shaly	1543	1080	65	1312	1148	0.429	0.353
P mode	sandy	1854	1631	58	1743	1806	0.137	0.128
	crs	*2132*	*1157*	*59*	*1645*	*1740*	*0.843*	*0.593*
Vibroseis	shaly	1448	1073	59	1261	1424	0.349	0.298
S mode	sandy	1891	1555	58	1723	1805	0.216	0.195
	crs	*1866*	*1754*	*85*	*1810*	*1775*	*0.064*	*0.062*

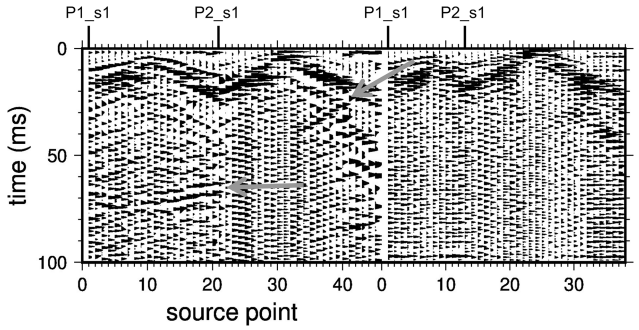

Figure 12. Receiver gather 8 from impact (left) and vibroseis-*P* (right) source operation. Grey arrows pointing to coherent events attributed to backscattered tunnel surface waves (~30 ms) and shear wave reflection event (~65 ms). The first shot point of the two profiles are marked (see Fig. 1 for profile and receiver locations). The data processing included bandpass filtering (150–500 Hz) and amplitude normalization (AGC 20 ms).

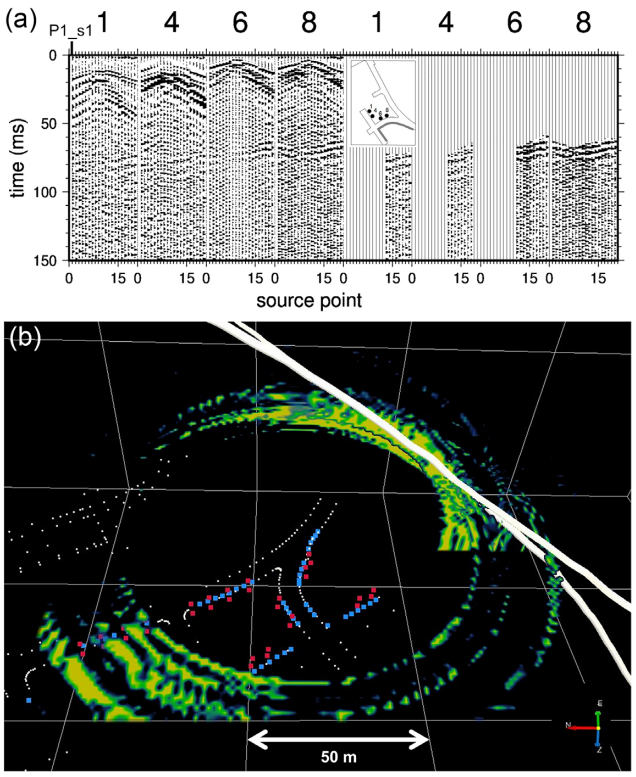

Figure 13. (a) Receiver gathers with reflection events before (left) and after (right) event extraction. The profile and receiver locations are outlined in the sketch of the laboratory. (b) 3-D perspective view of migrated shear wave reflections using the extracted event data with a homogeneous shear wave velocity (v_S = 1400 m s^{-1}) and projecting squared amplitudes. The gridline interval is 50 m. Legend: blue squares—shot points; red squares—receivers; white dots—tunnel outline; white thick lines—top upper shaly.

velocity axis correlates well with the bedding strike of the Opalinus Clay (Jaeggi *et al.* 2017). The shaly facies (v_{Pmax} = 3220 m s^{-1}, v_{Smax} = 1480 m s^{-1}) is characterized by slower velocities than the sandy (v_{Pmax} = 3720 m s^{-1}, v_{Smax} = 1840 m s^{-1}) and the carbonate-rich sandy facies (v_{Pmax} = 4000 m s^{-1}, v_{Smax} = 2050 m s^{-1}). In addition, the anisotropy results of the carbonate-rich sandy facies are poorly adapted, since they are based on only few rays and these rays propagated just along the fast velocity axis leading to an insufficient azimuthal coverage (Fig. 11). The seismic velocity anisotropy in the shaly facies (*AvP* = 23 per cent, *AvS* = 32 per cent) is much stronger than in the sandy facies (*AvP* = 9 per cent, *AvS* = 12 per cent) and it is more pronounced for shear waves than *P*-waves.

3.8. Suitability for structural imaging

The sparse and geometrically complex acquisition geometry of this experiment was mainly designed for time-efficient testing of different seismic sources and for traveltime and amplitude analyses of direct compressional and shear waves. In the receiver gathers (see examples in Fig. 12), we identified predominantly direct compressional and shear waves, as well as (tunnel) surface waves. In several receiver gathers, coherent phases were identified showing negative apparent velocities, which is usually a property of reflected tunnel surface waves, backscattered from structural features, such as niches or bifurcations of galleries. These backscattered tunnel surface waves are clearly observed on receiver gathers of impact data but almost invisible on receiver gathers of the vibroseis data. In Fig. 12, impact and vibroseis data show backscattered tunnel surface waves with a clearer signature in the impact source gather (see grey arrow pointing to event at ~30 ms). The impact source receiver gather shows an additional coherent event on the first 20 traces, which cannot be attributed to tunnel surface waves backscattered from structural features of the rock laboratory (arrow pointing to event at ~65 ms).

This coherent event can be identified on further impact source receiver gathers as shown in Fig. 13. Four gathers (receiver rods 1,

4, 6, and 8) are shown with coherent events between 60 and 75 ms. These events are attributed to a body wave reflection as the apparent velocities of these events are not related to the apparent velocities of direct or backscattered surface waves. In order to investigate the potential origin of these reflection events, we extracted them on the receiver gathers where they were visually identified. The extracted data are shown on the right hand side of Fig. 13 for receiver gathers 1, 4, 6, and 8. This event extraction was performed after bandpass filtering (150–500Hz) and without performing further amplitude gain in order to prevent artificial amplifications of processing artefacts. The reflection events can be clearly identified as laterally coherent events for the first 10 ms of the extracted event window. After these coherent phases, mostly incoherent noise is dominating the gathers. The extracted events were then migrated using a Kirchhoff pre-stack depth approach for three-component data, and assuming shear wave reflections. A homogeneous shear wave velocity (1400 m s $^{-1}$) was used for migration. The shear wave velocity of 1400 m s^{-1} corresponds to an approximate average value of v_S through the lower sandy and upper shaly facies of the Opalinus Clay (Section 3.7, Table 5). In order to avoid destructive interference of stacked amplitudes due to the simplified velocity model, squared amplitudes were projected into a 3-D volume around the acquisition area. The result is shown in Fig. 13(b). The 3-D image shows only amplitudes of the migrated volume which are above 80 per cent of the maximum amplitude, thus focusing onto the strongest reflectivity. Most of these strong amplitudes focus at a distance of ∼40–50m close to the predicted layer boundary between the Upper Shaly Facies and the Upper Sandy Facies of the Opalinus Clay, indicated by white lines in Fig. 13(b). The amplitudes are strongly smeared which is due to the sparseness of data, with some ghost reflections imaged on the lower left side of the figure. However, the concentration of strong reflectivity is largest close to the position of the layer boundary of the 'Top Upper Shaly Facies' of the Opalinus Clay, suggesting that the transition between shaly and sandy facies correlates with a large impedance contrast for shear waves. Previous high-resolution seismic investigations along boreholes through the sandy and shaly facies types of Opalinus Clay have found large velocity contrasts for compressional waves (Schuster *et al.* 2019). Anisotropic laboratory measurements on core samples indicated particularly high average differences of *P*-wave velocity perpendicular to the bedding direction (Siegesmund *et al.* 2014). Thus, the layer boundary between the Upper Shaly and the Upper Sandy Facies of the Opalinus Clay is obviously acting as a strongly reflecting structure which can be imaged by shear wave seismic reflection measurements.

4 DISCUSSION

4.1. In situ underground exploration systems—frequencies and observation ranges

Depending on the geotechnical task at hand, in situ measurements in boreholes or along tunnel walls utilize different source signals (impulse, vibrations, explosives) and frequency ranges. Small-scale investigation of the EDZ requires higher frequencies than transmission experiments at the facility scale. Furthermore, some tasks require non-invasive techniques that exclude explosive sources and borehole measurements.

A number of underground research laboratories (URL) are located in clay formations, e.g. Mont Terri, Tournemire, Meuse/Haute Marne, HADES etc. The vast majority of in situ seismic surveys conducted there are borehole measurements (single hole or cross-hole). The clay characterization is then valid in the immediate proximity of the borehole or between boreholes covering a decimeter to meter scale. However, if the task requires non-invasive techniques and boreholes cannot be conducted, a gallery-based acquisition is needed. Only very few gallery-based acquisitions occurred e.g. in the URL Tournemire or Mont Terri at the meso scale and they applied similar source types (impact and vibration sources). Zillmer *et al.* (2014) carried out seismic measurements using an ELVIS vibration source (Polom 2003; Krawczyk *et al.* 2012) on the tunnel floor to characterize the Toarcian claystone. Their survey comprised a frequency range from 60 Hz to 360 Hz and profile lengths of 74 m and 130 m. Bretaudeau *et al.* (2014) conducted a sledgehammer survey to characterize the Toarcian claystone and to detect fault zones within an area of a 100 m x 100 m by using full waveform inversion (FWI). The 3.5 kg sledgehammer generated signals with frequencies from 30 Hz to 1000 Hz and the maximum amplitude was found at a frequency of 400 Hz. Schuster *et al.* 2017 conducted seismic measurements in the Mont Terri (URL) to explore the Opalinus Clay using a multi-scale acquisition system (BGR) which includes mechanical impulse emitters and piezoelectric transducers. Their seismic transmission experiment was carried out between drifts and covered distances up to 60 m.

Although our study and the above-mentioned studies utilized similar source types, the characteristics of these sources are not the same. The sledgehammer and the impact source (this study) show a comparable frequency range in clay formations. However, the frequency range of the hit cannot be influenced unlike signals generated by vibration sources. In contrast to a manually driven sledgehammer, the mass of the impact source is released under high pressure (80 *g*) in controlled manner and that leads to a high repeatability of the source signal (see Section 3.2) which is essential for e.g. seismic monitoring. Vibration sources show also a high repeatability of the source signal. The ELVIS vibration source (Polom 2003; Krawczyk *et al.* 2012) and vibroseis source (this study) can both operate as *P*-wave and *S*-wave source. However, the operating principles of both *S*-wave sources differ. The head of the ELVIS-SH source oscillates directly in the horizontal direction, while the 2 heads of the vibroseis source oscillate with opposite phase. The frequency range and the peak force of the vibroseis source ($f = 0.2$–14 kHz, peak force ≈ 4270 N per actuator) are larger than those of the ELVIS source ($f = 20$–360 Hz, peak force ≈ 1100 N). The ELVIS source is mounted on a wheelbarrow and is operated on the floor, in contrast to vibroseis source which can be operated in arbitrary directions, i.e. on the floor or walls. The emitters of the mini-seismic system (Schuster *et al.* 2019) are able to excite frequencies from 1 to 100 kHz, but these high frequencies are intended for sonic and ultrasonic measurements. The vibroseis source focuses on the in situ underground exploration at the meso scale and therefore rely on signals with lower frequencies (<12 kHz) to ensure their propagation over deca- and hectometers. The adaptive and individual control of the two actuators that make up the vibroseis source results in particularly efficient transmission into the rock over a wide frequency range. The concept of combining multiple actuators which acts as one vibration source allows a further adaption on the exploration ranges, directions and resolution targets.

4.2. Comparison of vibroseis and impact source

This source comparison was performed using two different source types (a magnetostrictive vibroseis source and a pneumatic impact

source) of a gallery based seismic acquisition system (Giese *et al.* 2005). Although, the generation of *S*- waves with the vibroseis-*S* source is only partly successful, both *P*-wave sources (impact and vibroseis-*P*) operated successfully in the Opalinus Clay. In general, the recorded impact data display clearer waveforms than the vibroseis-*P* data what is reflected by higher SNR and lower frequencies of the impact data compared to the vibroseis data (Figs 4–6). The vibroseis source is attributed a better control of the frequency content of the signals due to predefined sweep signal and a feedback loop to adjust the amplitude and phase response of the outgoing signal (Krauß *et al.* 2014). But the adjustment of signal frequency and amplitude for specific tasks is limited by the bandwidth of the actuators and the medium characteristics. The construction of the actuators itself bounds frequencies downwards. Signals with frequencies below this characteristic line can be generated with great effort, but malfunctions can also occur. The characteristics of the medium and its quality at the tunnel wall limit frequencies upwards. High frequency signals generated at the tunnel wall can be absorbed, while high frequency signals emitted from a borehole nearby propagate successfully (pers. comm. R. Giese). Another issue arises with the acquisition setup itself. The receivers and the recording system (here DAQlinks) are usually coupled with cables, which makes the equipment sensitive to electromagnetic noise like an antenna. To reduce these disturbing effects on the data a high technical effort, e.g. shielding, electromagnetic decoupling of the acquisition, is required, since the magnitude of noise depends on various factors, e.g. number of receivers, DAQlinks, cable length, sweep length.

In general, clay formations are stronger attenuating than crystalline and salt formations and therefore more selective for frequencies above 300 Hz (Giese *et al.* 2021). Nonetheless, the applications of these sources in crystalline and salt rock confirm our findings in claystone: (1) The vibroseis-*P* source generated signals with broader amplitude spectra than the impact source (Fig. 6 and Richter *et al.* 2018). (2) The signal-to-noise ratio of the impact data is higher than the SNR of the vibroseis-*P* data (Fig. 5 and Richter *et al.* 2018). In addition, Richter *et al.* (2018) revealed that the penetration depth of the impact source (∼140 m) is higher than the penetration depth of the vibroseis-*P* source (∼120 m). In claystone, we also observe a larger penetration depth of the impact source compared to the vibroseis source (Fig. 12), but the penetration depth in claystone is smaller than in salt rock. However, we can only specify the minimum operating range in clay due to the limited acquisition layout of our study. To achieve far offsets in clay, signals with strong lower frequencies in the range of 50–500/600 Hz, as emitted from the impact source, are the most promising. Since the vibroseis source respond more sensitive to the medium than the impact source, its performance in clay is not perfect for far-offset applications. The absolute performances of both source types are dependent on the rock type, for example the frequency range or the penetration depth differs for different rocks. But the relative characteristics of the sources among each other remain the same, e.g. the impact source generates stronger lower frequencies than the vibroseis source. These different frequency characteristics of the sources lead to different excitation of surface waves, which are much more pronounced in the case of the impact source.

4.3. Attenuation

The Q estimation is based on assumptions that are not completely fulfilled in our study. For example, the source spectrum of the vibroseis data is approximated using the spectrum of synthetic sweep signal which does not include coupling effects with the rock. Since frequencies below 300 Hz are missing in the vibroseis data, also at near offsets, the slope fitting started at 300 Hz to make the sweep more realistic. In addition, our complex setting within an anisotropic medium might increase the uncertainty of the Q estimation. Therefore, we illustrated the variation of Q by error bars in Fig. 10. Taking these into account the results provide a range of Q for the Opalinus Clay.

The Q estimates derived from the shaly-crs data set analysed as a whole (Fig. 10a) are strongly dominated by the shaly facies. Isolating source-receiver combinations from the shaly facies results in relatively similar Q values (Fig. 10b) showing different Q values for EDZ affected areas and undisturbed rocks. Q estimates derived from the carbonate-rich sandy facies, which has a smaller data coverage and thus greater uncertainties, show larger values (>15) close to the tunnel wall correlating with a lower influence of the EDZ in the carbonate-rich sandy facies (Lanyon *et al.* 2014) and indicating the differences between the facies types. The median of Q_{impact} (∼16) is lower than the Q estimates of Le Gonidec *et al.* (2014), who derived a Q value of approximately 20 at the Mont Terri URL at the transition from the sandy (Ga08) to the upper shaly facies (Ga04). This low value corresponds to strongly attenuating media and sedimentary rocks (Jones 1995). Bretaudeau *et al.* (2014) determined Q by trial and error with numerical modelling of field measurements and revealed a Q value of 25 at the Tournemire URL. However, using ultrasonic and sonic measurements Zinszner *et al.* (2002) evaluated much higher Q estimates of 50–100 for the clay formation at the Tournemire URL. Although the mineralogy of Toarcian claystone (Tournemire) and Opalinus Clay (Mont Terri) are different (Bossart 2017), those studies emphasize the general vagueness of Q estimation at different scales.

4.4. Characterization of Opalinus Clay

Our clay characterization is based on picked *P*- and *S*-wave onset times, averaged *P*- and *S*-wave velocities and elliptical fits whose determinations entail uncertainties: Pick inaccuracy and straight ray approach result in velocity errors which propagate due to fitting inaccuracies. The rms deviations between our elliptical fits and our data (see Fig. 11) are ∼94–216 m s^{-1} for v_{P} (Fig. 14a) and 66–135 m s^{-1} for v_{S} (Fig. 14b). About 66–76 per cent of our *P*-data and 67–74 per cent of our *S*-data lie within this uncertainty range. If we double this range more than 90 per cent of our velocities are included. The largest rms deviation is found for the carbonate-rich sandy facies where the largest scattering occurred (Fig. 11).

Considering these uncertainties, the results of our clay characterization (*cf.* Section 3.7) are compared to the results of previous seismic investigations carried out in situ and in the laboratory (*cf.* Section 2.1, Fig. 14a). Due to our experimental setup and the bedding anisotropy of the Opalinus Clay, v_{min} is oriented with a deviation of ∼45° to the symmetry axis, while v_{max} is directly comparable to the velocities parallel to bedding. Schuster *et al.* (2017) performed a seismic transmission experiment (ST) and determined the seismic *P*-wave velocity parallel to bedding. For the carbonate-rich sandy facies, our results are almost equal to Schuster *et al.* (2017). However, we derived higher velocities (v_{Pmax}) for the sandy (∼300 m s^{-1}) and the shaly facies (∼200 m s^{-1}) than Schuster *et al.* (2017). But interval velocity measurements (IVM) performed in boreholes in the sandy facies show that the velocity along the borehole is strongly varying in the range of $v_{\mathrm{P}||} = 2600$–4600 m

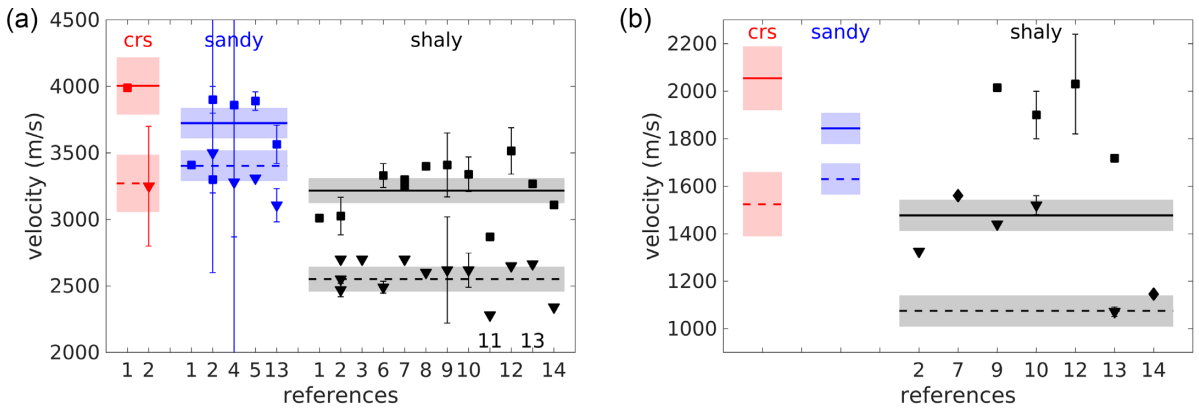

Figure 14. Comparison of our *P*-wave (a) and *S*-wave (b) velocities with published velocities of the Opalinus Clay. The estimated maximum (solid lines) and minimum (dotted lines) velocities are related to published velocities parallel (■) and normal (▼) to bedding. Published velocities with a different angle to bedding are marked as diamond (◆). The coloured areas mark the range of the rms deviation between fit and data (Fig. 11) that includes ∼66–76 per cent of the data. References: 1—ST, Schuster *et al.* (2017); 2—IVM, Schuster *et al.* (2017); 3—XHM, Schuster *et al.* (2017); 4—Gschwind (2013); 5—Siegesmund *et al.* (2014); 6—Nicollin *et al.* (2008); 7—Le Gonidec *et al.* (2012); 8—Jaeggi *et al.* (2017); 9—Popp & Salzer (2007); 10—Bock (2009); 11—Zappone *et al.* (2021); 12—Wenning *et al.* (2021); 13—Lozovyi & Bauer (2018); 14—Manukyan *et al.* (2012).

s^{-1} (Schuster *et al.* 2017). In addition, Schuster *et al.* (2017) used IVM to determine v_P normal to bedding and our v_{Pmin} lies within the range of $v_{P\perp} = 3200$–3800 m s^{-1}. The laboratory velocity measurements of Siegesmund *et al.* (2014) and Gschwind (2013) are almost equal and their $v_{P||}$ are ∼100 m s^{-1} larger, while $v_{P\perp}$ are ∼100 m s^{-1} slower than our velocities. The seismic velocity anisotropy *AvP* of Siegesmund *et al.* (2014) is 2–4 per cent larger than our *AvP*. The velocities of the shaly facies show the same trend than those of the sandy facies. Compared to Schuster *et al.* (2017), v_{Pmax} is faster than their $v_{P||}$ derived by IVM and ST, but about 100–200 m s^{-1} slower than $v_{P||}$ measured by Nicollin *et al.* (2008), Le Gonidec *et al.* (2012), Jaeggi *et al.* (2017), Lozovyi & Bauer (2018), Popp & Salzer (2007) and Bock (2009). v_{Pmin} is only faster than $v_{P\perp}$ of Nicollin *et al.* (2008) and some IVMs of Schuster *et al.* (2017). It is mainly about 100–200 m s^{-1} slower than $v_{P\perp}$ published by Popp & Salzer (2007), Bock (2009), Le Gonidec *et al.* (2012), Jaeggi *et al.* (2017), Lozovyi & Bauer (2018) and other IVMs of Schuster *et al.* (2017). In general, the velocity variations are up to ±200 m s^{-1}. Larger v_P differences (∼10 per cent) are found with respect to Zappone *et al.* (2021) or Manukyan *et al.* (2012). In terms of the seismic anisotropy, Popp & Salzer (2007) derived a seismic velocity anisotropy that is 2 per cent higher than ours; Wenning *et al.* (2021) determined an even 10 per cent higher *AvP*, while the Schuster *et al.* (2017) estimated anisotropy coefficients that are 3–6 per cent smaller than ours. Zappone *et al.* (2021) determined an anisotropy coefficient of 0.26 that is similar to ours. Since the anisotropy estimation is based on seismic velocities that differ from our values, these differences are expected. But they are rather small, given the high degree of overall heterogeneity of the facies.

In general, we observe that the resulting seismic velocities are faster in the sandy facies than in the shaly facies. This is consistent with Siegesmund *et al.* (2014) who already explained this by different facies compositions: The sandy facies has higher contents of carbonate and quartz and lower contents of clay minerals in contrast to the shaly facies (Klinkenberg *et al.* 2009; Kaufhold *et al.* 2013). The velocity determinations were based on various methods (tomographic studies, borehole measurements, ultrasonic measurements in the lab), that were performed at different scales (cm to m scale). In addition, the facies itself can be characterized by strong velocity changes, e.g. along a borehole. Applying the same method at different test sites within the same facies can reveal different velocities due to different clay compositions at the sites. Taking this into account combined with our estimated uncertainties (pick and fitting inaccuracy) and considering the deviation of the symmetry axis our results, derived at the meso scale using a low-invasive gallery-based method, and the published ones are in good agreement.

In contrast to *P*-wave velocities, only few *S*-wave velocities and anisotropy were found in the literature and they vary strongly for the shaly facies (Fig. 14b): The shear wave velocities ($v_{S||} = 1900 \pm 100$ m s^{-1}, $v_{S\perp} = 1520 \pm 40$ m s^{-1}) of Bock (2009) are equally high than those ($v_{S||} = 2015$ m s^{-1}, $v_{S\perp} = 1440$ m s^{-1}) of Popp & Salzer (2007) or those ($v_{S||} = 1820$–2240 m s^{-1}) of Wenning *et al.* (2021). But the shear wave velocities of Popp & Salzer (2007) and Bock (2009) are clearly higher compared to $v_{S||} = 1720$ m s^{-1} of Lozovyi & Bauer (2018) or $v_{S\perp} = 1325$ m s^{-1} of Schuster *et al.* (2017). Le Gonidec *et al.* (2012) determined a v_S of 1560 m s^{-1} with deviation of 30° to bedding. Our findings ($v_{Smax} = 1477$ m s^{-1}, $v_{Smin} = 1074$ m s^{-1}) are again smaller than those just mentioned and correlate well with an averaged v_S (1145 m s^{-1}) of Manukyan *et al.* (2012) and $v_{S\perp} = 1070$ m s^{-1} of Lozovyi & Bauer (2018). Lozovyi & Bauer (2018) performed a dispersion analysis for the Opalinus Clay with ultrasonic (500 kHz) and seismic frequencies (0.5–150 Hz). They found a significant velocity difference (∼200 m s^{-1}) for the different frequencies used. Since most of the v_S values were determined with lab and log studies, this finding can explain the deviations to some extent. Our resulting *AvS* of 32 per cent correlates with the *AvS* range of 30–40 per cent given by Popp & Salzer (2007). Since no shear wave velocities of the carbonate-rich sandy facies and sandy facies are found in the literature, our findings contribute to close this gap. In order to characterize the clay formations spatially, anisotropic tomographic imaging using our *P*- and *S*-wave data was performed (Esefelder *et al.* 2021). In spite of a sparse acquisition setup, the facies transition between shaly and carbonate-rich sandy facies was reproduced in the v_P and v_S distributions. In the Mont Terri project phase 26, the impact survey covering the shaly and carbonate-rich sandy facies was repeated

with a denser shot point interval. The additional shot points will improve the azimuthal coverage and consequently the estimation of the *P*- and *S*-wave anisotropy.

5 CONCLUSIONS

In this study, detailed results of a seismic survey, acquired in the Mont Terri URL (Switzerland) are presented, aiming at in situ exploration and characterization of argillaceous rocks. This task was accompanied by assessing the applicability of two different source types (magnetostrictive vibroseis and pneumatic impact source) in argillaceous formations and evaluating their performance at the meso scale under similar conditions. Our survey was a low to non-invasive approach with sources operating from the gallery (non-invasive) and receivers installed in short boreholes (low-invasive). The generated signals of both source types cover a similar bandwidth in Opalinus Clay, but the impact source generated lower frequencies ($f > 200$ Hz) than the vibroseis source ($f > 300$ Hz) and frequencies above 800 Hz are strongly attenuated. The excited energy and the accomplished penetration depth were sufficient for transmission and reflection imaging over several decameters. The impact source was at an advantage due to the higher signal-to-noise ratio.

The clay characterization confirmed the clearly distinguishable *P*- and *S*-wave velocities of the different facies types of the Opalinus Clay (see Tables 4 and 5) and the *P*-wave results agree well with other Mont Terri studies. Especially the shear wave results show a significant variation between laboratory and in situ studies. Since only few shear wave investigations were conducted at the meso scale, there exists no robust data base yet for comparison of field and lab data, so that our results increase the *S*-wave knowledge of the Opalinus Clay and its facies types. Our acquisition geometry was mainly designed for performing transmission experiments, but also for testing of different seismic source types. Most of the backscattered energy was traced back to structural features of the URL, i.e. niches or bifurcations of galleries. Nevertheless, coherent backscattered events could be extracted and were migrated using a pre-stack Kirchhoff depth approach. The strong amplitudes focus at a distance of ∼40–50 m and image the transition between the upper shaly and upper sandy facies whose location was extrapolated in the geological model.

The experimental results discussed in this study for clay confirm previous experiences made in underground exploration campaigns in crystalline and rock salt environments. Although, seismic underground exploration in clay formations is challenging due to strong attenuation and pronounced elastic anisotropy, sources providing strong and repeatable signals are appropriate for imaging between and around the underground infrastructure. For tomographic imaging as well as for reflection imaging at larger distances (∼50 m and more from the galleries and tunnels), impact sources with high repeatability should be preferred. Small vibroseis sources have the potential to generate specifically high frequency signals for imaging at high resolution and avoiding strong surface reverberations along the tunnels and galleries, but especially for high frequencies (>800 Hz in this study) their low penetration range must be considered.

As shown here, the combination of *P*-wave and *S*-wave measurements, as well as the adapted use of near-offset and far-offset surveying provide good possibilities for clay exploration in general.

ACKNOWLEDGMENTS

The authors acknowledge the financial support for the iCross project by the Federal Ministry of Education and Research (project number 02NUK053D), the Helmholtz Association and the GFZ. We are grateful for the technical support provided by Swisstopo, in particular by S. Schefer and D. Jaeggi. The field survey was carried out by the authors, J. Mach and with support of the Helmholtz Innovation Lab '3D-Underground Seismic' (A. Jurczyk, K. Krüger). The authors thank the editor and the two anonymous reviewers for their comments and suggestions that helped to improve the manuscript.

DATA AVAILABILITY

The data set used and analysed in this study will be available via the GFZ Data Services (https://doi.org/10.5880/GIPP.201999.1).

REFERENCES

Bäppler, K., 2018. Digitization in mechanized tunnelling technology, In *North American Tunneling Proceedings,* pp. 157–162, eds. Howard, A., Campbell, B., Penrice, D., Preedy, M. & Rush, J., Society for Mining, Metallurgy and Exploration.

Birch, F., 1961. The velocity of compressional waves in rocks to 10 kilobars, Part II, *J. geophys. Res.,* **66,** 2199–2224.

Bock, H., 2009. RA experiment: updated review of the rock mechanics properties of the opalinus clay of the Mont Terri URL based on laboratory and field testing, Technical Report 2008-04, Mont Terri project, www.mont-terri.ch.

Bohlen, T., Lorang, U., Rabbel, W., Müller, C., Giese, R., Lüth, S. & Jetschny, S., 2007. Rayleigh-to-shear wave conversion at the tunnel face - From 3D-FD modeling to ahead-of-drill exploration, *Geophysics,* **72**(6), T67–T79.

Bossart, P. *et al.*, 2017. Mont Terri rock laboratory, 20 years of research: introduction, site characteristics and overview of experiments, *Swiss J. Geosci.,* **110,** 3–22.

Bossart, P., 2017. Twenty years of research at the Mont Terri rock laboratory: what we have learnt, *Swiss J. Geosci.,* **110,** 405–411.

Bretaudeau, F., Gélis, C., Leparoux, D., Brossier, R., Cabrera, J. & Côte, P., 2014. High-resolution quantitative seismic imaging of a strike-slip fault with small vertical offset in clay rocks from underground galleries: experimental platform of Tournemire, France, *Geophysics,* **79,** B1–B18.

Cai, W., Dou, L., Cao, A., Gong, S. & Li, Z., 2014. Application of seismic velocity tomography in underground coal mines: a case study of Yima mining area, Henan, China, *J. Appl. Geophys.,* **109,** 140–149.

Cheng, F., Liu, J., Qu, N., Mao, M. & Zhou, L., 2014. Two-dimensional pre-stack reverse time imaging based on tunnel space, *J. Appl. Geophys.,* **104,** 106–113.

Dales, P., Audet, P., Olivier, G. & Mercier, J.-P., 2017. Interferometric methods for spatio temporal seismic monitoring in underground mines, *Geophys. J. Int.,* **210,** 731–742.

Dickmann, T. & Sander, B., 1996. Drivage concurrent tunnel seismic prediction, *Felsbau,* **14,** 406–411.

Dresen, L., 1985. Flözwellenseismik für die untertägige Steinkohlenerkundung, In *Methoden der Angewandten Geophysik und mathematische Verfahren in den Geowissenschaften, Band II,* ed. Bender, F., Ferdinand Enke Verlag.

Edelmann, H.A.K., 1981. SHOVER shear-wave generation by vibration orthogonal to the polarization, *Geophys. Prospect.,* **29,** 541–549.

Esefelder, R., Wawerzinek, B., Lüth, S., Giese, R. & Krawczyk, C.M., 2021. Seismic anisotropy of Opalinus Clay - Tomographic investigations at the scale of an underground rock laboratory (URL), *Swiss J. Geosci.,* **114,** 21.

Gal, O., 2003. fit_ellipse(https://www.mathworks.com/matlabcentral/fileexchange/3215-fit_ellipse), MATLAB Central File Exchange. Retrieved: May, 2019.

Giese, R., Klose, C.D. & Borm, G.W., 2005. In situ seismic investigations of fault zones in the Leventina Gneiss Complex of the Swiss

Central Alps, In *Petrophysical Properties of Crystalline Rocks,* Geological Society special publication 240, pp. 15–24, eds. Harvey, P.K., Brewer, T.S., Pezard, P.A. & Petrov, V.A., Geological Society. https://doi.org/10.1144/GSL.SP.2005.240.01.02.

Giese, R., Lüth, S., Richter, H., Wawerzinek, B., Jaksch, K. & Esefelder, R., 2021. 3D-Underground Seismics in crystalline, salt and clay rocks, *NSG2021 27th European Meeting of Environmental and Engineering Geophysics,* 1–5. https://doi.org/10.3997/2214-4609.202120046.

Gschwind, S., 2013. The relationship between failure behavior and sedimentary subfacies types in the sandy facies of Opalinus Clay, *Master's thesis*, Swiss Federal Institute of Technology in Zurich (ETH Zurich), Zurich, Switzerland.

Guglielmi, Y., Birkholzer, J., Rutqvist, J., Jeanne, P. & Nussbaum, C., 2017. Can Fault leakage occur before or without reactivation? Results from an in situ fault reactivation experiment at Mont Terri, *Energy Procedia,* **114,** 3167–3174.

IAEA, 2009. Geological disposal of radioactive waste: technological implications for retrievability, IAEA nuclear energy series, no. NW-T-1.19, ISSN 1995-7807.

Jaeggi, D., Laurich, B., Nussbaum, C., Schuster, K. & Connolly, P., 2017. Tectonic structure of the "Main Fault" in the Opalinus Clay, Mont Terri rock laboratory (Switzerland), *Swiss J. Geosci.,* **110,** 67–84.

Johnston, D.H., Toksöz, M.N. & Timur, A., 1979. Attenuation of seismic waves in dry and saturated rocks: II. Mechanisms, *Geophysics,* **44**(5), 691–711.

Jones, S.M., 1995. Velocity and quality factors of sedimentary rocks at low and effective pressure, *Geophys. J. Int.,* **123,** 774–780.

Kaufhold, A., Gräsle, W., Plischke, I., Dohrmann, R. & Siegesmund, S., 2013. Influence of carbonate content and microfabrics on the failure strength of the sandy facies of the Opalinus Clay from Mont Terri (Underground Research Laboratory), *Eng. Geol.,* **156,** 111–118.

Klinkenberg, M, Kaufhold, S., Dohrmann, R. & Siegesmund, S., 2009. Influence of carbonate microfabric on the failure strength of claystones, *Eng. Geol.,* **107,** 42–54.

Kneib, G., Kassel, A. & Lorenz, K., 2000. Automatic seismic prediction ahead of the tunnel boring machine, *First Break,* **18,** 295–302.

Krauß, F., Giese, R., Alexandrakis, C. & Buske, S., 2014. Seismic travel-time and attenuation tomography to characterize the excavation damaged zone and the surrounding rock mass of a newly excavated ramp and chamber, *Int. J. Rock Mech. Min. Sci.,* **70,** 524–532.

Krawczyk, C.M., Polom, U., Trabs, S. & Dahm, T., 2012. Sinkholes in the city of Hamburg—new urban shear-wave reflection seismic system enables high-resolution imaging of subrosion structures, *J. Appl. Geophys.,* **78,** 133–143.

Lanyon, G.W., Martin, D., Giger, S. & Marschall, P., 2014. Development and evolution of the Excavation Damaged Zone (EDZ) in the Opalinus Clay–A synopsis of the state of knowledge from Mont Terri, Nagra Working Report NAB 14-087.

Le Gonidec, Y. *et al.*, 2012. Field-scale acoustic investigation of damaged anisotropic shale during a gallery excavation, *Int. J. Rock Mech. Min. Sci.,* **51,** 136–148.

Le Gonidec, Y., Sarout, J., Wassermann, J. & Nussbaum, C., 2014. Damage initiation and propagation assessed from stress-induced microseismic events during mine-by test in the Opalinus Clay, *Geophys. J. Int.,* **198,** 126–139.

Leparoux, D., Côte, P., Gélis, C. & Cabrera-Nunez, J., 2012. EDZ characterization with surface wave analysis: an experimental and numerical study for defining feasibility in the context of the Tournemire platform (France), *Near Surf. Geophys.,* **10,** 401–411.

Lozovyi, S. & Bauer, A., 2018. Static and dynamic stiffness measurements with Opalinus Clay, *Geophys. Prospect.,* **67,** 997–1019.

Lüth, S., Giese, R., Otto, P., Krüger, K., Mielitz, S., Bohlen, T. & Dickmann, T., 2008. Seismic investigations of the Piora Basin using S-wave conversions at the tunnel face of the Piora adit (Gotthard Base Tunnel), *Int. J. Rock Mech. Min. Sci.,* **45,** 86–93.

Manukyan, E. & Maurer, H., 2020. Elastic vertically transversely isotropic full-waveform inversion using cross-gradient constraints—an application toward high-level radioactive waste repository monitoring, *Geophysics,* **85**(4), R313–R323.

Manukyan, E., Maurer, H., Marelli, S., Greenhalgh, S.A. & Green, A.G., 2012. Seismic monitoring of radioactive waste repositories, *Geophysics,* **77**(6), EN73–EN83.

Margrave, G.F., 2021. CREWES MATLAB Software Library (CMSL), https://www.crewes.org/ResearchLinks/FreeSoftware/. Last access: June 2021.

Mazurek, M., Gautschi, A., Marschall, P., Vigneron, G., Lebon, P. & Delay, J., 2008. Transferability of geoscientific information from various sources (study sites, underground rock laboratories, natural analogues) to support safety cases for radioactive waste repositories in argillaceous formations, *Phys. Chem. Earth, Parts A/B/C,* **33,** S95–S105.

Nicollin, F., Gibert, D., Bossart, P., Nussbaum, C. & Guervilly, C., 2008. Seismic tomography of the Excavation Damaged Zone of the Gallery 04 in the Mont Terri Rock Laboratory, *Geophys. J. Int.,* **172,** 226–239.

Petronio, L. & Poletto, F., 2002. Seismic-while-drilling by using tunnel boring machine noise, *Geophysics,* **67,** 1798–1809.

Pisconti, A., Plenkers, K., Philipp, J. & Thomas, C., 2020. Mapping lithological boundaries in mines with array seismology and in situ acoustic emission monitoring, *Geophys. J. Int.,* **220,** 59–70.

Polom, U., 2003. Schwingungserzeuger für seismische Anwendungen, Deutsches Patent- und Markenamt, Patentschrift Nr. 102 35 126 C1.

Popp, T. & Salzer, K., 2007. Anisotropy of seismic and mechanical properties of Opalinus Clay during triaxial deformation in a multi-anvil apparatus, *Phys. Chem. Earth,* **32,** 879–888.

Richter, H., Hock, S., Mikulla, S., Krüger, K., Lüth, S., Polom, U., Dickmann, T. & Giese, R., 2018. Comparison of pneumatic impact and magnetostrictive vibrator sources for near surface seismic imaging in geotechnical environments, *J. Appl. Geophys.,* **159,** 173–185.

Rivet, D., De Barros, L., Guglielmi, Y., Cappa, F., Castilla, R. & Henry, P., 2016. Seismic velocity changes associated with aseismic deformations of a fault stimulated by fluid injection, *Geophys. Res. Lett.,* **43,** 9563–9572.

Schuster, K. 2019. Mini-Seismic Methods for the in-situ characterization of clay rocks—Examples from URL Meuse/Haute-Marne (France) and HADES URF (Belgium), *Geomechanics for Energy and the Environment,* **17,** 16–28.

Schuster, K., Amann, F., Yong, S., Bossart, P. & Connolly, P., 2017. High-resolution mini-seismic methods applied in the Mont Terri rock laboratory (Switzerland), *Swiss J. Geosci.,* **110,** 213–231.

Schuster, K., Furche, M., Shao, H., Hesser, J., Hertzsch, J.-M., Gräsle, W. & Rebscher, D., 2019. Understanding the evolution of nuclear waste repositories by performing appropriate experiments – selected investigations at Mont Terri rock laboratory, *Adv. Geosci.,* **49,** 175–186.

Siegesmund, S., Popp, T., Kaufhold, A., Dohrmann, R., Gräsle, W., Hinkes, R. & Schulte-Kortnack, D., 2014. Seismic and mechanical properties of Opalinus Clay: comparison between sandy and shaly facies from Mont Terri (Switzerland), *Environ. Earth Sci.,* **71,** 3737–3749.

Sopher, D., Juhlin, C., Huang, F., Ivandic, M. & Lüth, S., 2014. Quantitative assessment of seismic source performance: feasibility of small and affordable seismic sources for long term monitoring at the Ketzin CO2 storage site, Germany, *J. Appl. Geophys.,* **107,** 171–186.

Staples, R.K., Hobbs, R.W. & White, R.S., 1999. A comparison between airguns and explosives as wide-angle seismic sources, *Geophys. Prospect.,* **47,** 313–339.

Toksöz, M.N., Johnston, D.H. & Timur, A., 1979. Attenuation of seismic waves in dry and saturated rocks: I. Laboratory measurements, *Geophysics,* **44**(5), 681–690.

Tonn, R. 1991. The determination of the seismic quality factor Q from VSP data: a comparison of different computational methods, *Geophysical Prospecting,* **39,** 1–27.

Tzavaras, J., Buske, S., Groß, K. & Shapiro, S., 2012. Three-dimensional seismic imaging of tunnels, *Int. J. Rock. Mech. Min. Sci.,* **49,** 12–20.

Wenning, Q.C. *et al.*, 2021. Shale fault zone structure and stress dependent anisotropic permeability and seismic velocity properties (Opalinus Clay, Switzerland), *J. Struct. Geol.,* **144,** 104273.

Yancey, D.J., Imhof, M.G., Feddock, J.E. & Gresham, T., 2007. Analysis and application of coal seam seismic waves for detecting abandoned mines, *Geophysics,* **72**(5), M7–M15.

Yordkayhun, S., Ivanova, A., Giese, R., Juhlin, C. & Cosma, C., 2009. Comparison of surface seismic sources at the CO2SINK site, Ketzin, Germany, *Geophys. Prospect.,* **57,** 125–139.

Zappone, A. *et al.*, 2021. Fault sealing and caprock integrity for CO2 storage: an in situ injection experiment, *Solid Earth,* **12,** 319–343.

Zillmer, M., Marthelot, J.-M., Gélis, C., Cabrera, J. & Druivenga, G., 2014. In situ seismic measurements in claystone at Tournemire (France), *Geophys. J. Int.,* **199,** 1798–1807.

Zinszner, B., Meynier, P., Cabrera, J. & Volant, P., 2002. Vitesse des ondes ultrasoniques, soniques et sismiques dans les argilites du tunnel de Tournemire. Effect de l'anisotropie et de la fracturation naturelle, *Oil Gas Sci. Technol. – Rev. IFP,* **57,** 341–353.